DESIGN AND ANALYSIS OF AIR AND COOLANT CONTROL

FOR A POLYMER ELECTROLYTE MEMBRANE FUEL CELL

Except where reference is made to the work of others, the work described in this thesis is my own or was done in collaboration with my advisory committee. This thesis does not include proprietary or classified information.

_____

Jong-Woo Ahn

Certificate of Approval:

_____   _____

David Beale   Song-Yul Choe, Chair
Professor   Associate Professor
Mechanical Engineering   Mechanical Engineering

_____   _____

George Flowers   Joe F. Pittman
Professor   Interim Dean
Mechanical Engineering   Graduate School

DESIGN AND ANALYSIS OF AIR AND COOLANT CONTROL

FOR A POLYMER ELECTROLYTE MEMBRANE FUEL CELL

Jong-Woo Ahn

A Thesis

Submitted to

the Graduate Faculty of

Auburn University

in Partial Fulfillment of the

Requirements for the

Degree of

Master of Science

Auburn, Alabama
August 4, 2007

DESIGN AND ANALYSIS OF AIR AND COOLANT CONTROL

FOR A POLYMER ELECTROLYTE MEMBRANE FUEL CELL

Jong-Woo Ahn

Permission is granted to Auburn University to make copies of this thesis at its discretion,
upon the request of individuals or institutions and at their expense.
The author reserves all publication rights.

_____

Signature of Author

_____

Date of Graduation

VITA

Jong-Woo Ahn, son of Hong-Kyu Ahn and Ok-Jae You, was born on July 13th, 1977 in Jinju, Gyeongnam, and the Republic of Korea. He entered Han-Kuk Aviation University in March, 1996 and earned a Bachelor of Engineering degree in the Aeronautical and Mechanical Engineering in Feb, 2002. In August 2004, He entered Illinois Institute of Technology to pursue a Master of Science degree in Department of Mechanical, Material & Aerospace Engineering. In May 2005, he transferred to Auburn University.

THESIS ABSTRACT

DESIGN AND ANALYSIS OF AIR AND COOLANT CONTROL

FOR A POLYMER ELECTROLYTE MEMBRANE FUEL CELL

Jong-Woo Ahn

Master of Science, August 4, 2007
(B.S., Han-Kuk Aviation University, 2002)

84 typed pages

Directed by Song-Yul Choe

The polymer electrolyte membrane (PEM) fuel cell is an alternative engine that can potentially replace the internal combustion engine in the vehicles of the future. When hydrogen, stored in a tank, and oxygen, from the air, chemically react in the PEM fuel cell, electricity is generated and water and heat are produced as byproducts. Air and thermal management of a PEM fuel cell system are two important issues for ensuring reliable operation and maintaining a high efficiency at continuously changing loads. Insufficient oxygen supply at dynamic loads on the cathode side causes oxygen starvation that can damage the thin layers of the cells. Conversely, excessive air supply increases the parasitic power dissipated by an air blower and this loss lowers the efficiency. Therefore, efforts to ensure the proper supply of oxygen have been proposed by different researchers who applied advanced control strategies that dynamically replenish the oxygen. However, those control strategies did not consider thermal effects.

When operating PEM fuel cell stacks, heat produced continuously changes as the load current varies. Variation of temperature in the cell directly affects the rate of chemical reactions and water transport. Improper rejection of the heat might produce local hotspots and destroy the thin layers of the cell components. Conversely, elevated temperatures facilitate removal of water produced in the catalysts and increase mobility of water vapor in the membrane, which alleviates over-potentials. In addition, reduction of the parasitic power necessary for operating the electrical coolant pump can increase the efficiency. Therefore, development of a temperature control strategy could help to resolve concerns about reliable and efficient operation. This research project describes the design and analysis of control strategies for an air and thermal system that should reject excessive heat in the stack, minimize the parasitic power, and prevent oxygen starvation in the air supply system. The thermal circuit considered consists of a bypass valve, a radiator with a fan, a reservoir and a coolant pump, while a blower, and inlet and outlet manifolds, are the components for the air supply system. Finally, a classic proportional and integral (PI) and a state feedback control for the thermal circuit have been designed. Disturbances are compensated by a feed-forward element. The entire system is simulated and analytical results of the dynamic behavior are presented.

ACKNOWLEDGEMENTS

Computer software used: Microsoft word 2003,

                             MATLAB/SIMULINK

TABLE OF CONTENTS

LIST OF FIGURES

LIST OF TABLES

NOMENCLATURE

Alphabets:		Units
A	Area	m^2
C	Mass concentration	$kg\ m^{-3}$
Cp	Specific heat	$J\ kg^{-1}\ K^{-1}$
h	Heat transfer coefficient	$W\ m^{-2}\ ^{-1}$
F	Faraday number	$A\ s\ mol^{-1}$
Fr	Radiator frontal area	m^2
i	Current density	$A\ cm^{-1}$
I	Current	A
J	Rotational inertia	$kg\ m^2$
m	Mass	kg
M	Molar mass	$kg\ mol^{-1}$
N	Molar flux	$mol\ s^{-1}\ m^{-3}$
p	Pressure (partial pressure)	Pa
Q	Heat	J
R	Universal gas constant	$J\ mol^{-1}\ K^{-1}$
R	Resistance	Ω
s	Entropy	$J\ mol^{-1}\ K^{-1}$
t	Thickness	m

T	Temperature	K
W	Mass flux	kg s^{-1} m^{-2}

Greeks:

ε	Porosity	
λ	Water uptake coefficient	
η	Efficiency	
ρ	Density	kg m^{-3}
σ	Conductivity	
τ	Tortuosity	
τ	Torque	
φ	Flux linkage	V s rad^{-1}

Superscripts, subscripts:

amb	Ambient air
an	Anode
bl	Blower
c	Coolant
ca	Cathode
catl	Catalyst layer
cv	Control volume
diff	Diffusion

elec   Electro

g   Gas

i   Index

m   Motor

membr   Membrane layer

pl   Pole

s   Stator

1. INTRODUCTION

1.1. FUEL CELL TECHNOLOGY

Fuel cell technology is one of the energy sources that could have the potential to replace the traditional internal combustion engine (ICE) because of its high efficiency and low emissions. The fuel cell is a chemical device that converts the chemical energy contained in fuels directly into electrical energy and ejects water, carbon dioxide, and heat as byproducts. The working principles of the ICE and the fuel cell are compared in Figure 1.
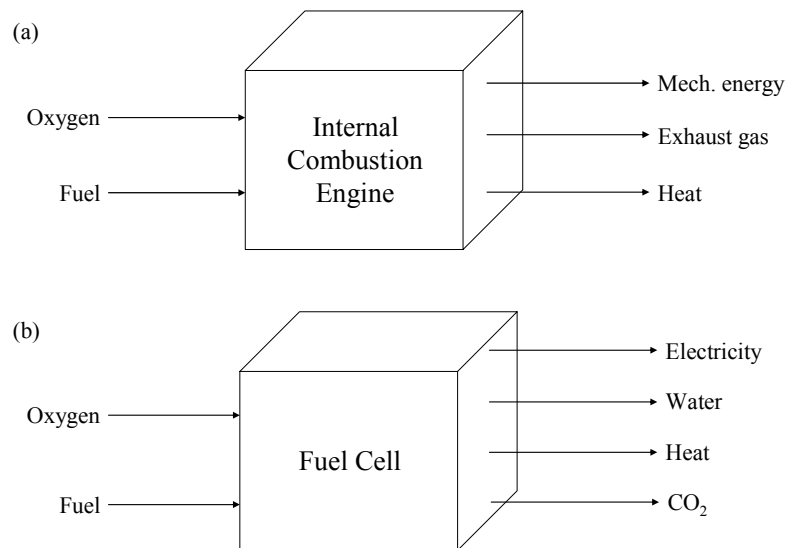
Figure 1 Principle of energy conversion for (a) Internal combustion engine and (b) fuel cell

Fuel cell technology can be classified by the type of electrolyte, fuel, and operating temperature. Different fuel cell technologies are summarized in Table 1 [1].

Fuel Cell Tpye	Electrolyte	Fuel	Operating temperature
PEMFC	Polymer membrane	H_2	30-100
DMFC	Polymer membrane	CH_3OH	20-90
PAFC	H_3PO_4	Natural gas	~220
MCFC	$Li_2CO_3\text{-}K_2CO_3$	Natural gas	~650
SOFC	Yttria-stabilized zirconia	H_2, CO,CH_4	500-1000

Table 1 Different fuel cell technologies

Fuel cell technologies have been used in a variety of applications as shown in Figure 2. Each type has its own advantages.
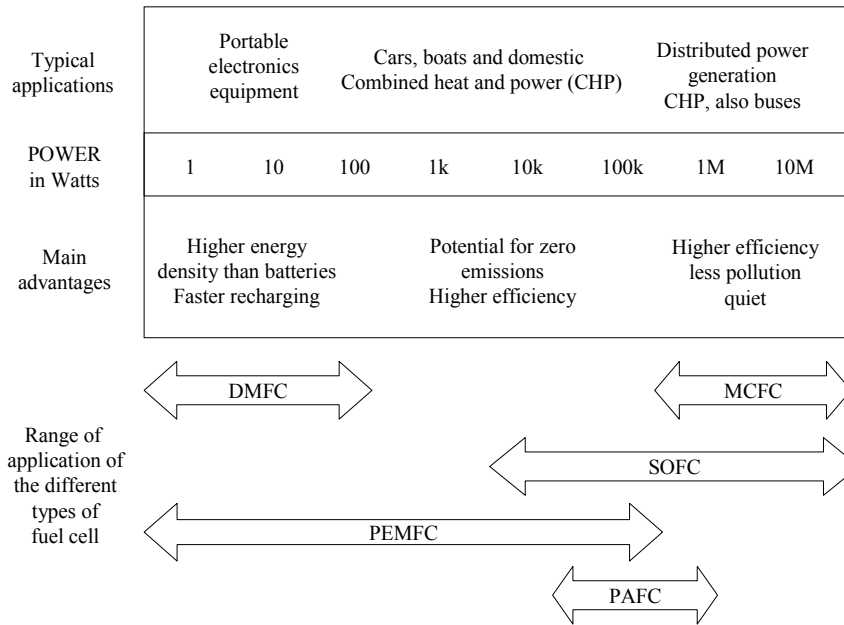
Figure 2 Applications and main advantages for different types of fuel cells [1]

The basis for the polymer electrolyte membrane fuel cell (PEMFC) is a solid polymer electrolyte that allows protons to be transported at the same time and electrons to

be blocked. When hydrogen is supplied on the anode side, oxidation occurs in the catalyst and molecules of hydrogen are separated into protons and electrons. When oxygen is supplied to the cathode side, reduction occurs in the catalyst with protons being transferred through the membrane and electrons being conducted through an external path. The reaction in the catalyst on the cathode side produces water and heat along with proton conductivity in the membrane. Because of the relatively low operating temperature, the PEMFC requires a precious material to dissolve molecules. Currently, platinum (Pt) or alloys with platinum and carbon supports are used for the catalysts. Even with the high costs of precious materials, the PEMFC is regarded as the most viable of the fuel cell technologies because of its fast start-up time, low operating temperature, and relatively high power density.

The principle of the direct methanol fuel cell (DMFC) is similar to that of the PEMFC. However, the DMFC produces electricity through an electrochemical process without converting methanol into hydrogen. At the anode, methanol with water is split into protons that pass through the membrane to the cathode, carbon dioxides, and the electrons that transport through an external circuit to the cathode. At the cathode, the oxygen combined with protons being transferred through the membrane and electrons being conducted through an external circuit. The chemical reaction produces water and heat in the catalyst on the cathode side. Because of the high energy required for oxidation on the anode side, the chemical reaction rate is relatively slow. Thus, the power density of the DMFC is much lower than that of the PEMFC. In addition, the catalysts are likely to become poisoned by the carbon monoxide produced. However, liquid methanol can be

easily stored, recharged, and discharged. Thus, the DMFC can be used as a power source in portable electronic devices.

The phosphoric acid fuel cell (PAFC) is similar to the PEMFC except it requires phosphoric acid as the electrolyte. The phosphoric acid has a low ionic conductivity at low temperatures, so the PAFC's operating temperature is ~150°C-200°C. At this operating temperature, the water generated is vaporized. When the heat carried by the water vapor is reused for heating space and water, the overall efficiency can reach 80% in combined heat and power applications. However, an external reformer is necessary to remove carbon monoxide residing in feeding fuels that can likely poison platinum or Pt alloys used for catalysts.

The molten carbonate fuel cell (MCFC) uses a molten mixture of alkali metal carbonates as electrolyte, which forms molten salts containing carbonate ions at high-temperature. At the cathode, oxygen reacts with the carbon dioxide and the electrons produced in the anode and produces carbonate ions, which are transferred from the cathode to the anode side. At the anode, the carbonate ions are converted into carbon dioxide by reaction with hydrogen producing water and electrons. The electrons travel through an external circuit to the cathode. The MCFC operates at ~650°C, so no precious metal is necessary for its catalysts. Thus, fuel flexibility is much higher for the MCFC than for the other technologies.

The solid oxide fuel cell (SOFC) is also different from the PEMFC. The SOFC uses a solid ceramic electrolyte, which transports negatively charged ions from the

cathode to the anode. When oxygen is supplied to the cathode, reduction occurs in the catalyst and the electrons flow through an external path with oxygen ions transferred through the electrolyte. When hydrogen is supplied on the anode side, the oxidation reaction between oxygen ions and hydrogen occurs in the catalyst and produces water and electricity. The high operating temperature (~600-1000°C) means that precious metals do not need to be used as catalysts, which allows for high flexibility in the choice of fuels. In addition, heat can be reused in combined heat and power applications (CHP), and thus the technology is the most efficient of those discussed. However, the start-up time is slow because of the thermal mass and sealing the cell is one of the challenging issues that must be overcome to ensure reliable operation.

1.2   OPERATING PRINCIPLE OF THE FUEL CELL

The electrochemical reactions occurring in a fuel cell depend upon the type of fuel cell. However, the fundamental concept is the same as that of the PEMFC. A typical PEM fuel cell is constructed with various layers: a gas channel serves to provide pathways for hydrogen and air to the fuel cell. The reactants are evenly distributed through a gas distribution layer (GDL) and react in the catalyst layer contacting the GDL. The membrane located in the middle of the fuel cell separates the anode and the cathode, while conducting the protons and blocking electrons. Within the PEMFC, the hydrogen and the oxygen react to form water and produce electricity, while heat is generated.

The overall chemical reaction can be expressed:

$$H_2 + \frac{1}{2}O_2 \rightarrow H_2O \tag{1}$$

In fact, the chemical reaction occurs at two electrodes. While the oxygen combines with protons and forms water at the cathode side, the hydrogen is oxidized and split to yield protons and electrons at the anode side. A schematic diagram of the electrochemical reaction in a fuel cell is shown in Figure 3.
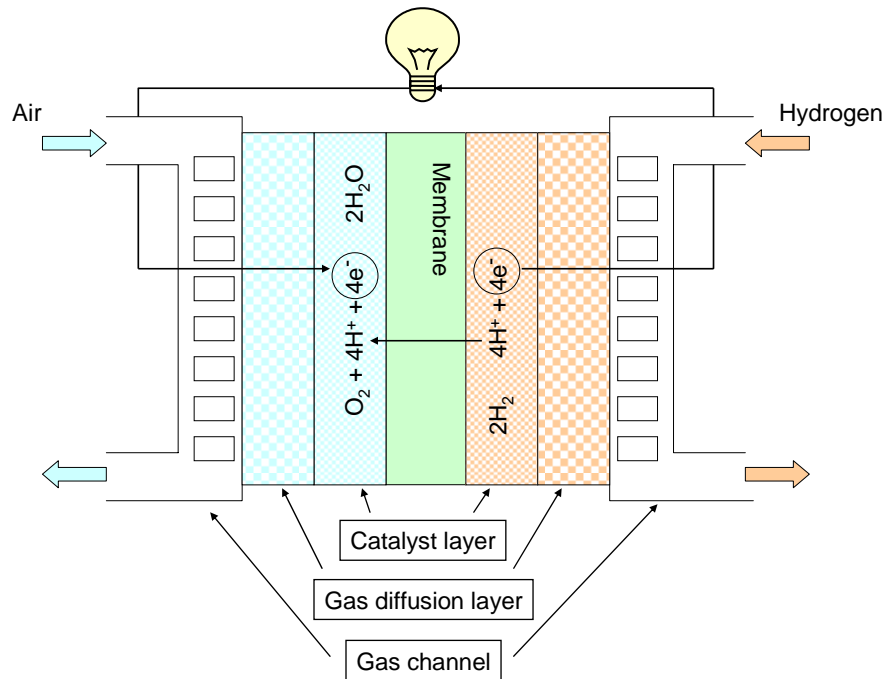
Figure 3 Schematic representation of a PEM fuel cell

1.3. PEM FUEL CELL SYSTEM

1.3.1. STACK MODEL

The stack model used in this thesis was derived on the basis of empirical equations and takes into account three additional major effects: the water balance in the membrane, the gas dynamics in the gas diffusion layer, and the temperature distribution in the cell (described below).

6

A cell is constructed by the connection of individual models in layers. The I-V characteristic is obtained by calculating the difference between the open circuit voltage and the over-potentials that include the ohmic over-potential in the membrane, the activation over-potential in the catalyst on the cathode side, and the concentration over-potential. The relationship for a single cell is a function of physical parameters such as the reactant partial pressure, temperature, current, and membrane water content [2]. The output characteristic of the stack is calculated as the product number times of a single cell.

$$V_{cell} = E(p,T) - v_{act}(p,T,i) - v_{ohmic}(i, \lambda_{membr}, T) - v_{conc}(p,T,i)$$
$$V_{st} = n \cdot V_{cell}$$

(2)

The dynamics of a fuel cell system involves the mass flow of air and water. The mass flow rate of the air at the cathode is equal to the sum of the mass flow of oxygen and nitrogen, which can be resolved into the sum of all masses in a control volume according to the mass conservation equation. Likewise, the mass variation of the vapor can be described by the changes in a control volume:

$$\dot{m}_{air} = \dot{m}_{O_2} + \dot{m}_{N_2}$$
$$\dot{m}_{O_2} = W_{O_2,in} - W_{O_2,out} - \dot{m}_{O_2,reacted}$$
$$\dot{m}_{N_2} = W_{N_2,in} - W_{N_2,out}$$
$$\dot{m}_{w,ca} = W_{v,in} - W_{v,out} + \dot{m}_{v,gen} + W_{v,membr}$$

(3)

in which,

$$\dot{m}_{O_2,reacted} = M_{O_2} \cdot \frac{nI_{st}}{4F}$$

$$\dot{m}_{v,gen} = M_v \cdot \frac{nI_{st}}{2F}$$

7

where M_{O_2} and M_v are oxygen and vapor molar mass, respectively.

In the same manner, the mass flow at the anode can be described by an equation (4):

$$\dot{m}_{H_2} = W_{H_2,in} - W_{H_2,out} - \dot{m}_{H_2,reacted}$$
$$\dot{m}_{w,an} = W_{v,an,in} - W_{v,an,out} + W_{v,membr}$$

(4)

where $\dot{m}_{H_2,reacted} = M_{H_2} \cdot \dfrac{nI_{st}}{2F}$, M_{H_2} represents the hydrogen molar mass.

The air supplied flows through the gas flow channel and the GDL before reaching the catalysts and at the same time takes up water from the humidifier. Water generated in the catalysts diffuses through the membrane, and protons take water from the anode to the cathode side. Heat generated by chemical reactions and charge transport elevates the temperature in the cell. All of these factors affect the dynamic behavior of the cell. Therefore, further improvements of the dynamics have been made by considering three factors: 1) the water dynamics in the membrane, 2) the partial pressure drop in the GDL, and 3) the temperature variation.

The dynamics of the water content that determines the proton conductivity is described by two components: the electro-osmotic driving force caused by the different electrochemical potentials at the anode and cathode, and the diffusion caused by the water concentration gradient at the two boundaries. Because the water mass flows at the boundaries of the membrane layer, the dynamics of the water concentration in the membrane can be improved as shown in equation (Eq.) 5 [3], where C is the mass

8

concentration (kg·m^{-3}), M is the mole mass (kg·mol^{-1}), b is the parameter given in reference [4], ρ is the membrane dry density, and A_{cell} is the fuel cell area (m^2):

$$\lambda_{membr} = \frac{C_{H_2O,mass} / M_{H_2O}}{\dfrac{\rho_{dry,membr}}{M_{membr}} - b \cdot C_{H_2O,mass} / M_{H_2O}}$$

$$\dot{m}_{water,membr} = \frac{d\left(C_{H_2O,mass} A_{cell} t_{membr}\right)}{dt} \tag{5}$$

$$= W_{ele,membr,an} - W_{ele,membr,ca} + W_{diff,membr,an} + W_{diff,membr,ca}$$

The reactants entering the cell diffuse through the GDL before reaching the catalyst layer, which significantly affects overall dynamics of the reactants. This diffusion effect is described by using the mass continuity and the Stefan-Maxwell equations (6) [5]:

$$\frac{\varepsilon_g}{RT} \frac{\partial p_i}{\partial t} + \frac{\partial N_i}{\partial y} = 0$$

$$\frac{\varepsilon_g}{\tau^2} \frac{\partial p_i}{\partial y} = \sum_{k=1}^{3} \frac{RT}{p_{ca} D_{ik}} \left(p_i N_k - p_k N_i\right) \tag{6}$$

Hence, $i, k \in (1, 3)$, where p_1 is the oxygen partial pressure, and $p_2 = p_{sat}(T)$ and p_3 are the water vapor and the nitrogen partial pressure, respectively; and the diffusion coefficients of $p_{ca} D_{ik}$ include the cathode pressure of p_{ca}, summing the species partial pressures. The parameters τ and ε_g are constants describing the pore curvature of the GDL.

If a cell is assembled from layers with isotropic and constant thermo-physical properties, the energy conservation equation shows that the total energy change in a

controlled volume is equal to the sum of energy exchange at the boundaries and the internal energy resources. In fact, the energy exchanges at the boundaries occur in two ways: by conduction across the cell or by convection between bipolar plates and the coolant, the reactants and water. Thus, the thermal-dynamic behavior can be described with the following energy conservation equation (7) [3]:

$$\sum_i Cp_i C_{i,mass} A_{cell} t_{cv} \frac{dT_{cv}}{dt} = \underbrace{\sum W_{in} A_{cell} Cp_j (T_{in} - T_{cv})}_{mass\ flow\ in} + \underbrace{\dot{Q}_{conv} A_{cell}}_{convection\ heat\ transfer}$$
$$+ \underbrace{\dot{Q}_{cond} A_{cell}}_{conduction\ heat\ transfer} + \underbrace{\dot{Q}_{sou}}_{sources} \tag{7}$$

The internal energy source is comprised of the entropy loss and the chemical energy required for protons to overcome the barrier of the over-potentials in both of the catalyst layers (8). In addition, other loses are ohmic losses caused by transport of electrons and protons in the cell [6]:

$$\dot{Q}_{sou} = I \cdot \left(-\frac{T\Delta s}{4F} + v_{act} + I \cdot R_{membr} \right) \tag{8}$$

where Δs is equal to -65.0 (J·mol^{-1}K^{-1}) [7], v_{act}, is given in reference [8], and R_{membr} is the membrane resistance.

1.3.2. BALANCE OF PLANT MODEL

The balance-of-plant (BOP) is the system of components necessary to supply reactants, remove heat generated, manage water produced, and control the actuators. Typical components needed for operating a PEM fuel cell system are a hydrogen tank to store fuels, an air blower along with inlet and outlet manifolds and a humidifier to supply

humidified oxygen, and finally a bypass valve, a radiator with a fan, a reservoir, a coolant pump, several control valves and controllers to properly manage the heat generated. A typical configuration is shown in Figure 4.
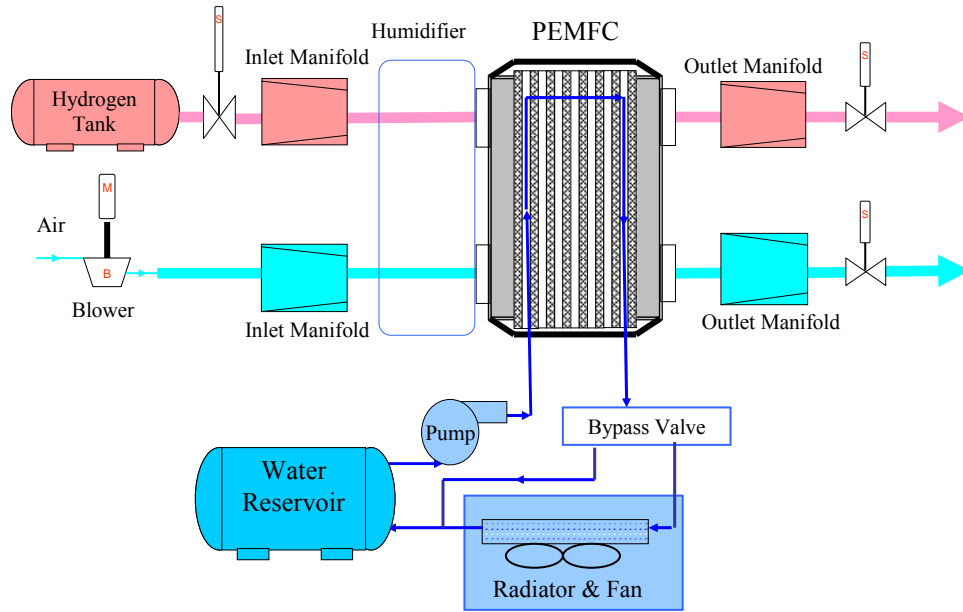
Figure 4 A schematic diagram of a PEM fuel cell system

1.3.2.1. AIR SUPPLY SYSTEM MODEL

The air supply system consists of four subsystems: an air blower, a humidifier, inlet and outlet manifolds, and a regulator to adjust the pressure in the stack. The blower is usually driven by an electric motor. The dynamic characteristic of the blower system is described by the sum of all moments of the inertia of the motor and the impeller, and the torque produced by the motor. Hence, the torque produced by the motor, $\tau_{bl,m}$ (J), is a

function of the stator resistance, $R_{s,bl,m}$ (Ohm), flux linkage, $\Phi_{bl,m}$ (V·s·rad⁻¹), the number

of the poles, $n_{bl,m,pl}$, and the stator voltage, $V_{bl,m}$ (V) [8]:

$$
\frac{d\omega_{bl}}{dt} = \frac{1}{J_{bl}} \left(\tau_{bl,m} - \frac{W_{bl}\Delta P_{bl}\eta_{bl,m}}{\eta_{bl}\rho_{amb}\omega_{bl}} \right)
$$

$$
\tau_{bl,m} = \eta_{bl,m} \frac{3}{2} \left(\frac{n_{bl,m,pl}}{2} \right) \left(\frac{\Phi_{bl,m}}{R_{s,bl,m}} \right) \left[V_{bl,m} - \left(\frac{N_{bl,m,pl}}{2} \right) \Phi_{bl,m}\omega_{bl} \right]
$$

(9)

where ω is angular velocity (rad·s⁻¹), J is rotational inertia (kg·m²), η is efficiency, p is

pressure (Pa), and ρ is air density (kg·m⁻³). The flow rate of the air blower is given as a

function of the angular velocity and pressure, and the efficiency is given as a function of

the flow rate and the angular velocity [9]:

$$
W_{bl} = \begin{cases} \omega_{bl} \cdot \left(-20.581 \cdot \left(p^* \right)^2 - 1.4415 \cdot 10^{-3} \cdot p^* + 4.1333 \cdot 10^{-5} \right), & p^* \leq 9 \cdot 10^{-4} \ Pa \cdot s^2 / rad^2 \\ otherwise, \ \omega_{bl} \cdot \left(-1.7973 \cdot p^* + 1.6409 \cdot 10^{-3} \right) \end{cases}
$$

(10)

$$
\eta_{bl} = -2.8831 \cdot 10^{13} \cdot \left(\frac{W_{bl}}{\omega_{bl}} \right)^3 + 9.5115 \cdot 10^8 \cdot \left(\frac{W_{bl}}{\omega_{bl}} \right)^2 + 1.3087 \cdot 10^4 \cdot \left(\frac{W_{bl}}{\omega_{bl}} \right) + 0.17945
$$

(11)

where p^* is $\left(\dfrac{P_{ca} - P_{amb}}{\omega_{bl}^2} \right)$.

The parameters of the blower were extracted by characteristic data and

specifications delivered by PADT (Phoenix Analysis & Design Technologies) [10],

which includes both the flow parameter and overall efficiency versus the head parameter.

The PEM fuel cell system uses a bubble-type or a membrane-type humidifier. The

bubble-type humidifier allows the air supplied to flow through the water for

humidification. By contrast, the membrane-type humidifier uses the stack outlet gas to

humidify the air. The water contained in the outlet gas is transported to the air supply

12

through a membrane. However, the humidifier in this study is simplified, and is represented as an ideal, without any associated dynamics and energy losses. The dynamic characteristics of the inlet and outlet manifold pressures are described by using the mass conservation equation, ideal gas law, and thermodynamic properties:

$$\frac{dp_{im}}{dt} = \frac{\gamma R_a}{V_{im}}\left(W_{bl}T_{bl} - W_{im,out}T_{im}\right)$$
$$\frac{dp_{om}}{dt} = \frac{R_a T_{om}}{V_{om}}\left(W_{ca,out} - W_{om,out}\right)$$

(12)

where γ is the specific heat (J kg^{-1} K^{-1}).

1.3.2.2. THERMAL CIRCUIT COMPONENTS MODEL

A thermal circuit should be capable of rejecting excessive heat produced by the stack. The circuit consists of a three-way valve to allow the coolant to bypass or to flow into a radiator to exchange heat with the ambient media, a fan to increase effectiveness of the heat convection, and a reservoir to store and to thermally insulate the coolants. Finally, a coolant pump serves to supply the coolant to the heat source.

If the opening of the bypass valve is assumed to be linear with a factor k, the coolant temperature at the reservoir inlet is expressed as a function of k, the coolant temperature at the stack outlet, $T_{st,c,out}$, and the radiator outlet, $T_{rad,c,out}$.

$$W_c \cdot Cp_c \cdot T_{res,c,in} = (1-k) \cdot W_c \cdot Cp_c \cdot T_{st,c,out} + k \cdot W_c \cdot Cp_c \cdot T_{rad,c,out}$$

(13)

The behavior of the radiator is described by the principles of thermodynamics. Kroger [11] proposed an empirical equation for a heat transfer coefficient of the radiator, h_{rad} (kW·m^{-2} $^{-1}$) and pressure drop, p_r (kPa) of the radiator as a function of the air flow

rate, W_{air} (kg·s^{-1}) [6]:

$$h_{rad} = -1.4495 \cdot W_{air}^2 + 5.9045 \cdot W_{air} - 0.1157$$
$$p_r = (326.12 \cdot W_{air} - 75.396) + 101.325 \qquad (14)$$

If the heat of the coolant is fully transferred to the radiator without any losses, the heat capacity of the coolant is identical with that of the radiator. Thus, the radiator outlet coolant temperature can be expressed as a function of the radiator geometry and the heat convection caused by the temperature difference between the ambient air temperature and the radiator outgoing air temperature [6]:

$$T_{rad,c,out} = T_{rad,c,in} - 0.5 \cdot \left(\frac{Fr_{area} \cdot (T_{rad,c,in} - T_{amb}) \cdot h_{rad}}{W_c Cp_c} \right) \qquad (15)$$

Where Fr_{area} denotes the frontal area (m^2) of the radiator and $T_{rad,c,in}$ denotes the radiator inlet coolant temperature. The electric power for the fan can be calculated according to a thermal dynamic relationship between the pressure drop and the air flow rate [6]:

$$P_{fan} = \frac{1}{\eta_{elec}\eta_{fan}} \left(W_{air} Cp_{air} T_{amb} P_r^{\left(\frac{k-1}{k}-1\right)} \right) \qquad (16)$$

where P_{fan} denotes the electric power (W) of the fan.

The reservoir should be thermally insulated after a heat exchange at the radiator by convection. The variation of the heat in the reservoir is the sum of the heat that the coolant carries and the heat being exchanged with the ambient air. Therefore, the reservoir outlet coolant temperature at the end of a given time interval, $T_{res,c,out}$ (K) can be expressed by the following equation [6]:

$$T_{res,c,out} = T_{res,p} - \frac{\Delta t}{mCp_{res}} (W_c Cp_c \cdot (T_{res,p} - T_{res,c,in}) + hA_{pl} \cdot (T_{res,c,in} - T_{amb})) \qquad (17)$$

where $T_{res,p}$ is the temperature of the reservoir at the previous time step (K), Δt is the time interval (s), mCp_{res} is the heat capacity of the reservoir (kg), $T_{res,c,in}$ is the reservoir inlet coolant temperature (K) and hA_{pl} is the heat transfer of plumbing to the ambient air (J·K⁻¹).

If all of the heat generated in the stack is completely transferred to the coolant, the coolant flow rate is governed by its relationship with the heat source:

$$W_c = \frac{\dot{Q}_{sou}}{Cp_c \Delta T} \qquad (18)$$

where ΔT is the temperature difference between the stack inlet and outlet coolants.

1.4.   THESIS OBJECTIVES

The PEM fuel cell system is a potential candidate to replace the ICE. Since the loads for the system are continuously changing, the air supplied and heat produced should be properly controlled to ensure safe and durable operation. Consequently, the objectives of this thesis are to identify control strategies for the air flow and coolant flow that optimally deliver the air and reject the heat produced in the stack and at the same time minimize parasitic power. To accomplish these objectives, dynamic models of the components have been developed and the associated controls designed. Finally, simulations were conducted to analyze the effects of the controls on the performance of the stack for varying loads.

The objectives of this thesis are to develop models of PEM fuel cells:

15

- To maintain the optimal air supply ratio,

- To improve the dynamics of the air supply at abrupt loads,

- To increase cooling effectiveness, and

- To maximize the total power by reducing parasitic power.

2.   LITERATURE REVIEW

Modeling of a plant is crucial for designing controls. The complexity of the working mechanism of the PEM fuel cell requires comprehensive models for the stack and the components necessary for operating the stack. Different mathematical approaches have been used to describe the dynamic behavior of a stack. These efforts fall into two categories: empirical equations having the I-V characteristic of a single cell (Guzzella [12] and Pischinger et al [13]) and the use of the computational fluid dynamics (CFD). The models based on the CFD have been widely used for understanding the mechanism of a single cell and studying parametric effects on performance. However, these methods have been inadequate for designing controls, because of the high computational time and the difficulty in extracting plant parameters for state equations.

Recently, Pukrushpan et al. [2] proposed a dynamic lumped model for a stack that has been used for designing controls for an air supply system. The stack is simply modeled by the multiplication of the number of cells and the characteristic of a single cell using empirical equations. In addition, the model includes dynamics of water, reactants on the cathode side, and a compressor by considering the moment of the inertia of rotating parts along with mass flow in the manifold.

Recently, Muller and Stefanopoulou [14] proposed a thermal dynamic model for a thermal management system that was experimentally verified. The model predicts the stack temperature and voltage as a function of the current drawn and inlet coolant conditions. In addition, the model for the gas supply system also included air and hydrogen flow components. However, diffusion of reactants and the influence of heat produced from chemical reactions were not fully considered. Shan and Choe [3] proposed a highly dynamic stack model that includes temperature effects on cell performance, water dynamics in the membrane, and diffusion of reactants in the GDL.

Proper control strategies are necessary for maximizing the performance of a fuel cell system and preventing any possible damage caused by oxygen starvation or overheating. Many publications have presented different control methodologies for air supply systems. Rodatz [14] proposed a dynamic model for a compressor that takes into account the dynamics of the compressor and inlet and outlet manifold filling processes. On the basis of this model, a regulator was designed by using the Linear Quadratic Gaussian (LQG) means and compared to a PI controller. The result showed that the use of the LGQ significantly improved the response time of the air supply.

Pukrushpan, et al. [16] proposed different control strategies for an air supply system to maintain the optimal oxygen excess ratio: the ratio between the amount of oxygen consumed and the amount of oxygen supplied. A static feed-forward control (SFF) and a feedback control (SFB) were employed to increase the oxygen excess ratio at any load applied and to improve recovery dynamics. The advanced controller gains were

optimized by using the Linear Quadratic Gaussian (LQG).

Vahidi [17] addressed the phenomenon of oxygen starvation, where the air cannot be delivered quickly to the fuel cell (at the instant the current changes) because the air flow rate is limited by the dynamics of the inlet manifold and the operational constraints of the compressor. Hybridization with a battery was proposed to minimize oxygen starvation and level a peak load. Optimal balance of the two sources was maintained by model predictive control (MPC).

Most of the research conducted for improved fuel cell system models and controls has focused on the air supply system, and has not considered the effects of temperature on the air supply system and the performance of the stack. On the basis of the energy balance and dynamics, Gurski [6] proposed models for components of the thermal circuit, including lumped models for a radiator, a fan and a coolant pump.

3.   AIR SUPPLY CONTROL

The stack model assumes that the reactants are fully humidified and that the working temperature in the stack is constant. In addition, it is assumed that no difference in partial pressure across the membrane exists. Under these assumptions, the reactants can only be controlled through the air supply system on the cathode side. When the stack current is suddenly drawn, the oxygen consumption increases. Thus, the oxygen partial pressure will drop, which causes a depletion of the oxygen on the cathode side and may potentially damage the catalyst. Therefore, the air supply system must continuously replenish the air to the cathode to allow the stack to follow the current command as quickly as possible. To better evaluate the dynamic supply of oxygen, the oxygen excess ratio was introduced as a new variable.

3.1. DESIGN OF AIR SUPPLY CONTROLLER

3.1.1. CONTROL CONFIGURATION

The mathematical description of the stack and the air supply system that consists of a blower and manifolds shows strong nonlinear characteristics that should be linearized to design a linear controller [2]. The linearized equations can be defined with state equations as follows:

$$x = \begin{bmatrix} m_{O_2}, & m_{H_2}, & m_{N_2}, & \omega_{bl}, & p_{im}, & m_{im}, & m_{w,an}, & p_{om} \end{bmatrix} \qquad \text{(States)}$$

$u = V_{BL}$ (Control input)

$w = I_{st}$ (Disturbance)

$y = \begin{bmatrix} W_{bl}, & P_{im}, & V_{st} \end{bmatrix}$ (Output)

$z = \begin{bmatrix} z_1 = P_{net}, & z_2 = \lambda_{O_2} \end{bmatrix}$ (Performance variables)

The system described above contains 8 states: m_{O2}, mass of oxygen in the cathode (g); m_{H2}, mass of hydrogen in the anode (g); m_{N2}, mass of nitrogen in the cathode (g); ω_{bl}, speed of the blower (kRPM); p_{im}, pressure of inlet manifold (bar); m_{im}, mass of air in the inlet manifold (g); $m_{w,an}$, mass of water in the anode (g); and p_{om}, pressure of outlet manifold (bar). The control input is the voltage of the blower motor, V_{bl} (V), and the stack current, I_{st} (A), is regarded as disturbance. The output includes: W_{bl}, air flow rate through the blower (g/s); P_{im}, pressure of inlet manifold (bar); and V_{st}, stack voltage (V). The performance variables are the net power (kW), P_{net}, and the oxygen excess ratio, λ_{O2}.

Figure 5 depicts two control configurations for the air supply system that employ a static feed-forward controller (SFF) and a feedback controller with a static feed-forward controller (SFB). The current is the reference for the system, which is generated from the output power of the stack necessary for the system.
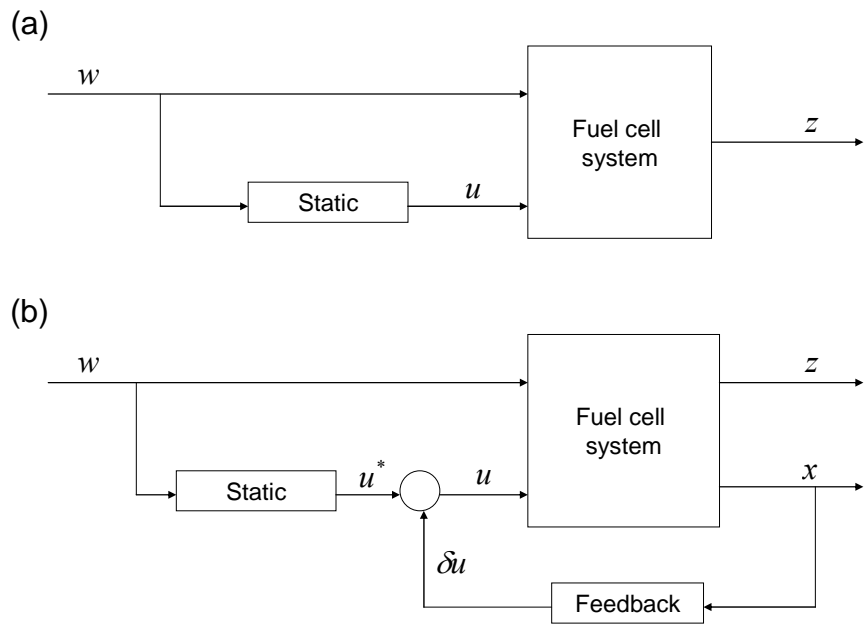
Figure 5 Control configurations of (a) a static feed-forward controller and (b) a feedback controller with a static feed-forward controller

3.1.2. STATIC FEED-FORWARD CONTROLLER

The reference current is usually used to calculate the flow rate of the fuels, which presents an open-loop control. The static feed-forward controller (SFF) makes use of the relationship between the reference current to an optimal blower motor voltage that should maintain the desired oxygen excess ratio of 2. This relationship is graphically depicted in Figure 6.
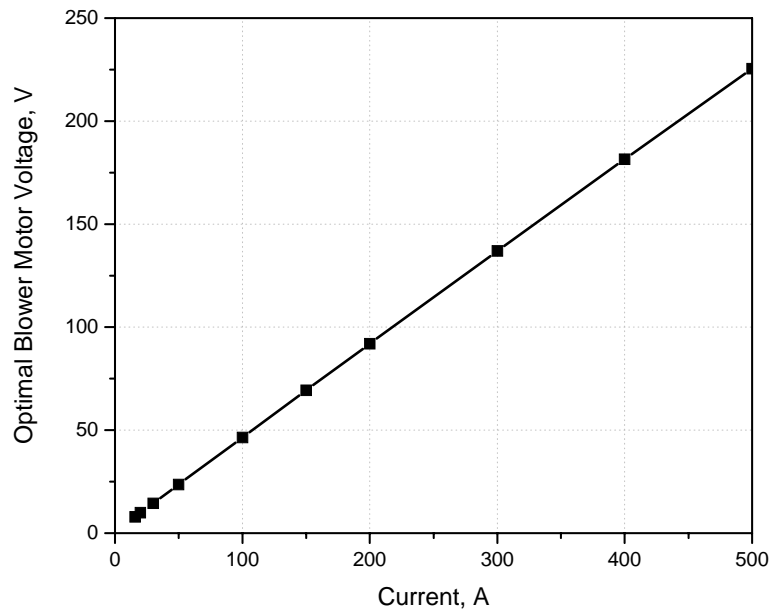
Figure 6 Optimal blower motor voltage for the static feed-forward controller

3.1.3. FEEDBACK CONTROLLER WITH STATIC FEED-FORWARD

The SFF shows an excellent dynamic response in rejection of the disturbance, but still has a steady state error. The error can be removed by employing a feedback controller, such as a PI controller that continuously compensates errors on the basis of the states measured. The errors of the reference values for the air flow rate and the state variables are amplified by a PI controller and added to the blower motor voltage given by the SFF as shown in Figure 7.

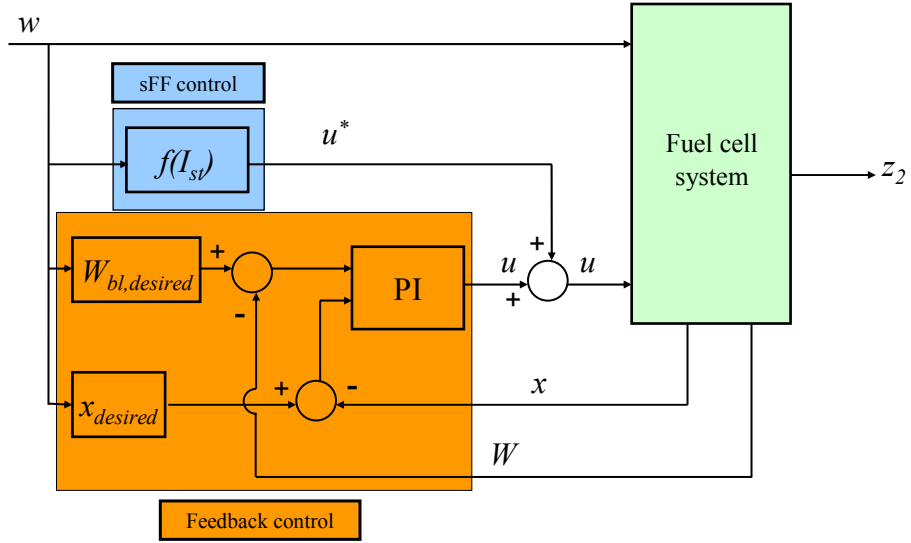Figure 7 Block diagram for the feedback control with a feed-forward

Since the state equations 3, 4, 9 and 12 of the fuel cell system are nonlinear [16], a linearization was performed at an operating point: where maximal net power, $P_{net}^{max} = 40kW$, the oxygen excess ratio, $\lambda_{O2}^{opt} = 2$, the stack current, $w^o = I_{st} = 191A$, and the blower motor voltage, $u^o = V_{BL}^{opt} = 164V$.

A general form of linearized state variable equations is expressed as follows:

$$\delta\dot{x} = A\delta x + B_u\delta u + B_w\delta w$$
$$\delta z = C_z\delta x + D_{zu}\delta u + D_{zw}\delta w \qquad (19)$$
$$\delta y = C_y\delta x + D_{yu}\delta u + D_{yw}\delta w$$

where δ denotes the derivative operator at an operating point.

The matrix values of the linearized system, including A, B_u, B_w, C_z, D_{zu}, D_{zw}, C_y, D_{yu} and D_{yw} are listed in Appendix A.

The linear quadratic regulator (LQR) [18] is widely used for optimization of the control gains, which basically sums the square of the errors. The gains become optimal if the cost function of the LQR (J) is a minimum value:

$$J = \int_0^\infty (\delta z_2^T Q_z \delta z_2 + q^T Q_I q + \delta u^T R \delta u) dt \tag{20}$$

where Q_z and Q_I represent the weighting factors amplifying the errors of the control objects, while the other weighting factor (R) is used to suppress the effect of the manipulating variable. In fact, the variable δz_2 includes the disturbance δw (Eq. 19) and the cost function. If the disturbance term in Eq. 19 is set to zero, the variable δz_2 yields a new variable with $\delta z_2' = C_{z_2} \delta x$ that is reflected in the cost function J (Eq. 21):

$$J = \int_0^\infty (\delta x^T C_{z_2}^T Q_z C_{z_2} \delta x + q^T Q_I q + \delta u^T R \delta u) dt \tag{21}$$

Consequently, the cost function includes a control input as well as the objects. If the control input is substituted by the function of a controller, the cost function will include control objects, which facilitates a determination of both weighting matrices that are only dependent upon the control objects. Eq. 22 describes the control input as a function of the control objectives:

$$\delta u = -K \begin{bmatrix} \delta \tilde{x} & q \end{bmatrix}^T = -K_p \delta \tilde{x} - K_I q \tag{22}$$

where $\delta \tilde{x} = \delta x_{desired} - \delta x$ and K represents the gain for the PI controller. The reference value of the state variables is $\delta x_{desired}$ and is obtained at $\delta z / \delta w = 0$. According to the optimal control theory, the variation of the cost function at a fixed end time can be derived:

$$\bar{J} = \int_0^\infty (\delta x^T C_{z_2}^T Q_z C_{z_2} \delta x + q^T Q_I q + \delta u^T R \delta u + \lambda^T (f(\delta x, \delta u, \delta w) - \delta \dot{x})) dt \tag{23}$$

where λ is defined as a co-state vector that can be an arbitrary value set because the variation of the cost function vanishes along an optimal trajectory. The last term, $-\int_0^\infty \lambda^T \delta \ddot{x} dt$, in Eq. 23 can be resolved into three parts, where the first and the second term are zeros because of the assumed initial and terminal fixed conditions:

$$-\int_0^\infty \lambda^T \delta \ddot{x} dt = -\lambda^T \delta \dot{x}(\infty) + \lambda^T \delta \dot{x}(0) + \int_0^\infty \dot{\lambda}^T \delta x \delta t \tag{24}$$

Finally, Eq. 24 is resolved into three parts, state, output and control input variables:

$$\delta \bar{J} = \int_0^\infty (\delta x^T C_{z_2}^T Q_z C_{z_2} + \lambda^T f_x + \dot{\lambda}^T) \delta x + (q^T Q_I + \lambda^T f_w) q + (\delta u^T R + \lambda^T f_u) \delta u) dt \tag{25}$$

where $f_x = -\int_0^\infty \lambda^T \delta \ddot{x} dt = -\lambda^T \delta \dot{x}(\infty) + \lambda^T \delta \dot{x}(0) + \int_0^\infty \dot{\lambda}^T \delta x \delta t = A$, $f_u = B_u$ and $f_w = B_w$.

If the cost function is minimized, each of the three terms in the variation of the cost function (Eq. 25) is equal to zero: $-\int_0^\infty \lambda^T \delta \ddot{x} dt = -\lambda^T \delta \dot{x}(\infty) + \lambda^T \delta \dot{x}(0) + \int_0^\infty \dot{\lambda}^T \delta x \delta t$

$$\dot{\lambda} = -C_{z_2} Q_z C_{z_2}^T \delta x - A^T \lambda \tag{26}$$

$$Q_I \delta w + B_w^T \lambda = 0 \tag{27}$$

$$R \delta u + B_u^T \lambda = 0 \tag{28}$$

If $\lambda = P\delta x$, then Eq. 26, 27 and 28 can be extended by Eq. 19, which results in the following equations:

$$PA + A^T P + C_{z_2} Q_z C_{z_2} - PB_u R^{-1} B_u^T P - PB_w Q_I^{-1} B_w^T P = 0 \tag{29}$$

Finally, the Algebraic Riccati equation (Eq. 29) is obtained, which can be solved by a MATLAB function (LQR). As a result, the gain for the PI controller is obtained from Eq. 26 and Eq. 27 with P:

$$\delta u = -R^{-1}B_u^T P \delta x - Q_I^{-1}B_w^T Pq = -K_p \delta \tilde{x} - K_I q \tag{30}$$

The weighting factor Q_I only affects the integrator gain. When Q_I increases, its influence on the cost function becomes larger, which leads to a large value of δz_2. Consequently, the dynamic response of the recovery behavior of the oxygen excess ratio becomes faster and achieves a steady state, but with an overshoot. Figure 8 shows the dynamic response of the δz_2 at different weighting factors, Q_I. In contrast, the weighting factor Q_z hardly improves the transition behavior as seen in Figure 9.
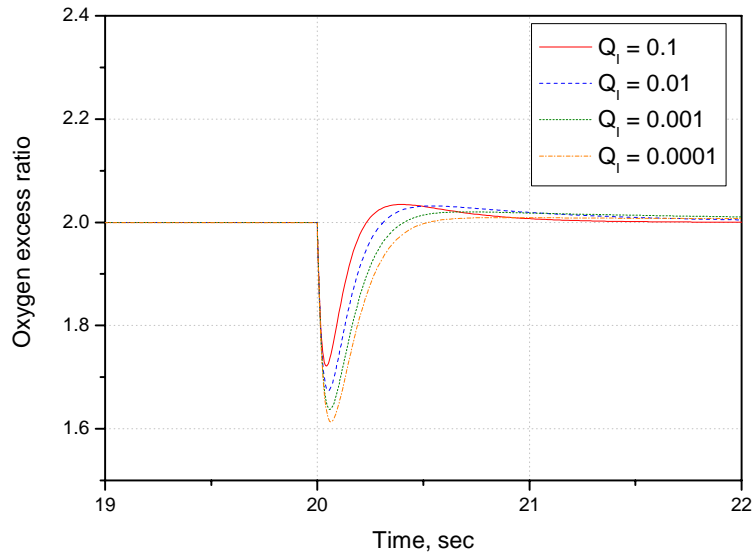

Figure 8 Effect of the weighting factor Q_I on the recovery behavior of the oxygen excess ratio
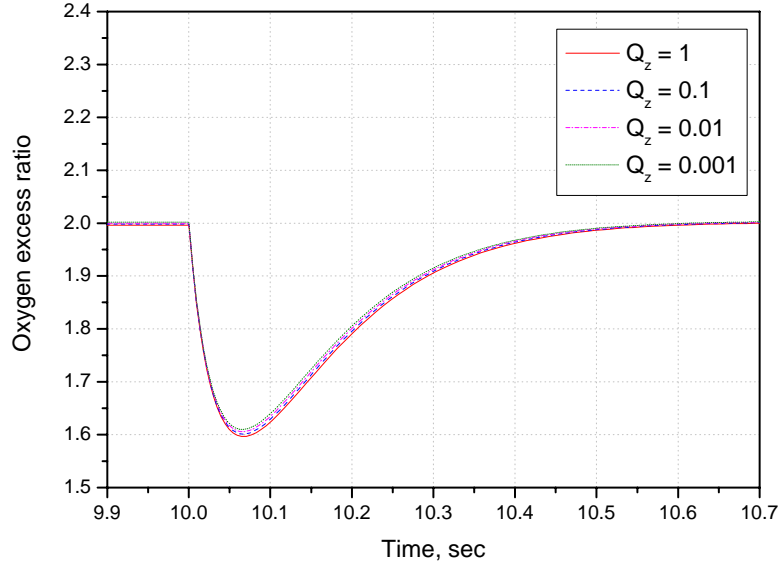
Figure 9 Effect of the weighting factor Q_z on the oxygen excess ratio

The optimum values of the weighting factors are $Q_z = 1$ and $Q_I = 0.01$. The gains for the PI controller are obtained accordingly, where the second and the seventh state variable are zeros. Both variables are related to the mass of the hydrogen and water on the anode side, which are assumed to be proportionally delivered:

$$K_p = \begin{bmatrix} -1.1060 \times 10^5 & 0 & -1.2636 \times 10^5 & 20.717 & 2.7681 \times 10^3 & -0.0019 & 0 & 33.5587 \end{bmatrix}$$
$$K_I = -3.1623$$

(31)

## 3.2. SIMULATION AND ANALYSIS

Simulations were performed to analyze the dynamic behavior of the stack along with the air supply. Dynamics of oxygen excess ratio and responses at the load currents were analyzed. The parameters and reference data for the models chosen are as follows (Table 2), which are partially empirical [2], [5], [6] and [19]. All models were coded by blocks given in MATLAB/Simulink.

28

Fuel Cell			Electrochemical Reation Model [2]		
n	382		P_0	1.0	Bar
A_{fc}	0.028	m^2	T_{ref}	353.15	K
Proton Conducting Model [19]			E_{ref}	1.229	V
b_{11}	0.5139		$A_{catl,eff}/A_{cell}$	$f(I, T, P_{o2})$	
b_{12}	0.326		Thermal model [6]		
b_2	350		H_{gas}	$f(P, T)$	
n_d	$f(C_{water})$		Cp_{gas}	$f(P, T)$	
D_w	$f(T, C_{water})$		ρ_{gas}	$f(P, T)$	
Gas Tranport Model [5]			Fr_{area}	2	m^2
Deff	$f(P, T)$	m^2s^{-1}	m_{res}	5	kg
Psat	$f(T)$		hA_{pl}	16.66	$J K^{-1}$

Table 2 Simulation parameters

Figure 10 demonstrates a comparison of responses at current steps between the SFF and the SFB using the PI controller. Here, the use of the PI controller rejects the disturbance better than SFF, where the recovery time for λ_{O_2} is reduced. The recovery time for the PI controller was 0.37 sec, while that for SFF was 0.85 sec. In addition, the PI controller minimizes the oxygen excess ratio drop as compared to that observed with the SFF control. The use of the PI controller is more effective and maintains the optimal oxygen excess ratio more efficiently than the SFF.
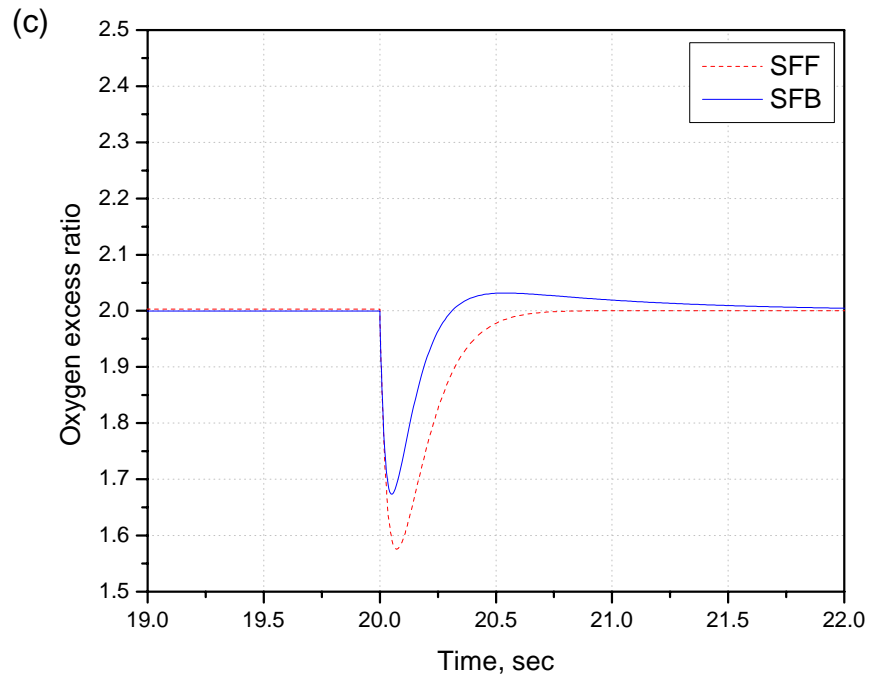
(a)

(b)
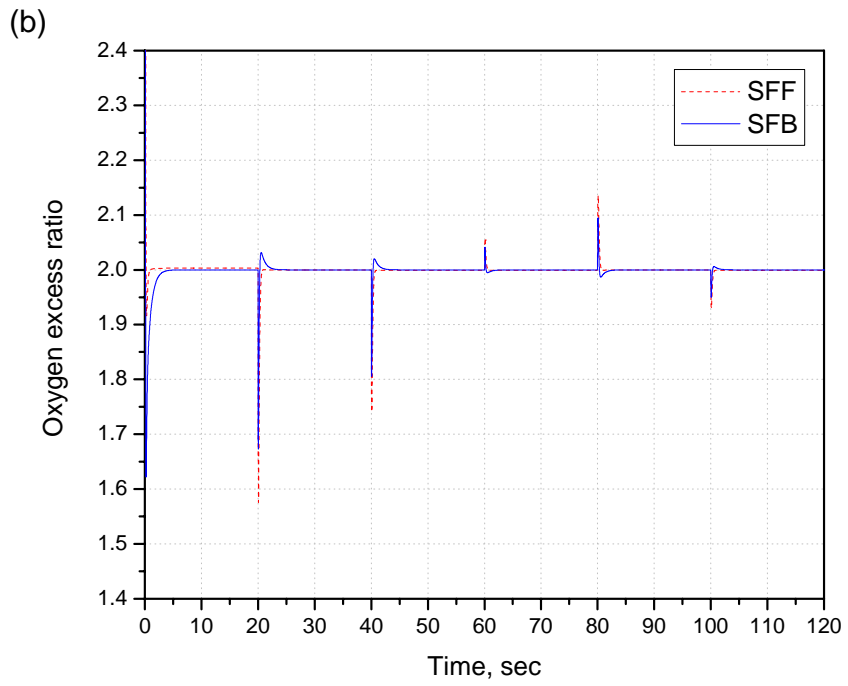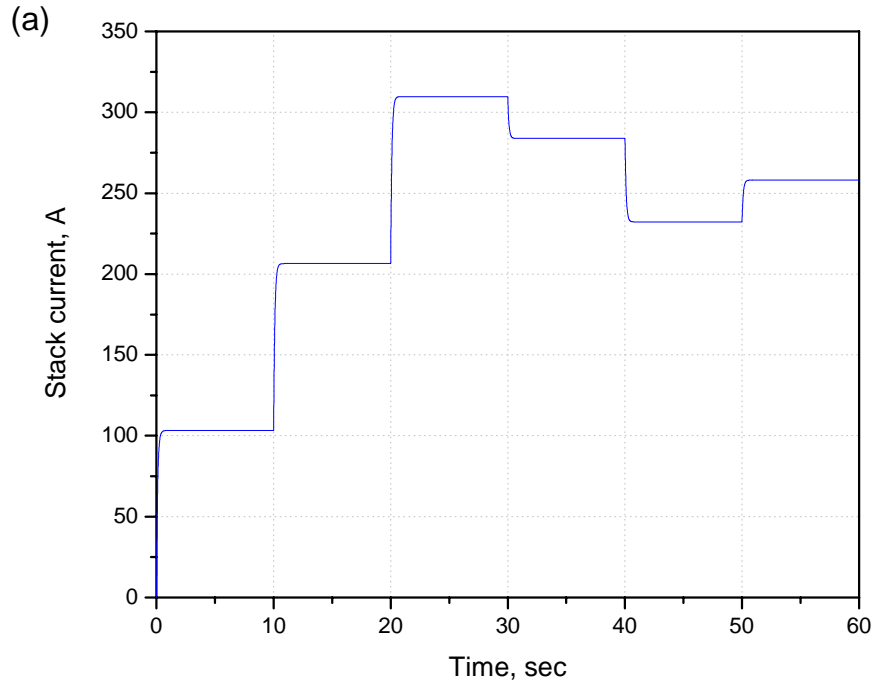
Figure 10 Comparison between SFF and SFB (a) reference load current (b) oxygen excess ratio (c) enlarged dynamic behavior of the oxygen excess ratio

4.   COOLANT CONTROL

The thermal circuit serves to reject excess heat generated in the stack. Currently, either bang-bang or linear PI controllers (Figure 11) are used to keep the temperature of the coolant constant. These controllers do not consider the optimization of parasitic power dissipated in the BOP components. The optimal operating temperature recommended for the PEM fuel cell stack is $80^{\circ}C$, which should be the peak value inside a cell. Earlier studies showed that the temperature in the catalysts on the cathode side is $3\text{-}8^{\circ}C$ higher than the average temperature of a stack [3]. Thus, the temperature of the coolant is controlled at $\sim70^{\circ}C$ (a safe temperature range for the stack). As a result, the reaction rate and efficiency are lower.

In the following sections, two new controls were designed and analyzed under several assumptions: the load current drawn for the stack is 0.5 A/cm^2, the air is fully humidified, the hydrogen flow rate supplied is proportional to the air flow rate, the temperature drop in the coolant pump is negligible, and no heat transfer occurs between the water reservoir and the ambient air. In addition, because it is not possible to measure the temperature in the catalyst layers, where most chemical reactions occur, the actual temperature of the stack is determined by averaging the outlet coolant temperatures of the

anode and cathode side. The reference temperature of the stack was raised to 76°C for the design of new controllers.
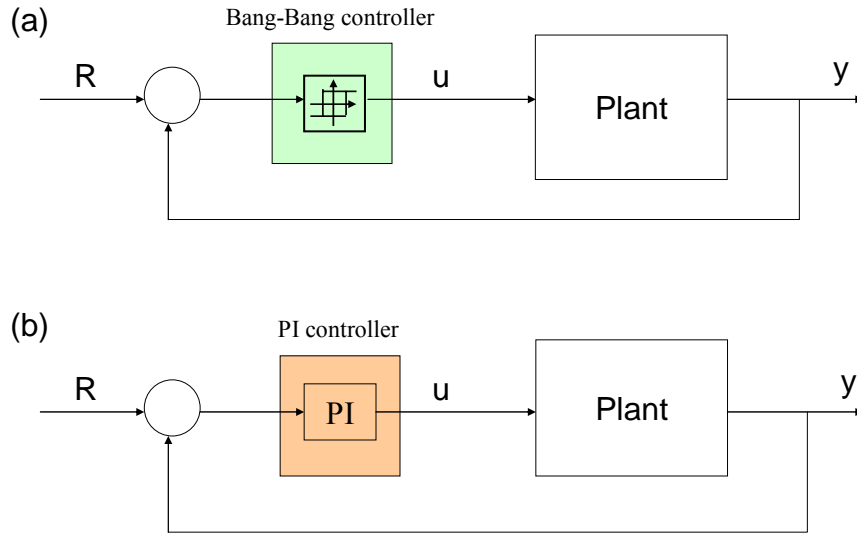

(a) Bang-Bang controller

(b) PI controller

Figure 11 Block diagrams of (a) Bang-Bang and (b) PI controllers

4.1.   PARAMETERS FOR THE THERMAL CIRCUIT

At equilibrium, the excess heat rejected by the coolants is identical with the sum of the heat the reservoir stores and the radiator exchanges with the ambient air. Once the maximum heat produced in the stack is given, then the relationship between a maximum coolant flow rate and the temperature rise along the coolant flow channel can be expressed:

$$\dot{Q}_{sou}^{\max} = W_c^{\max} \cdot Cp_c \cdot \Delta T \tag{32}$$

If $W_c^{\max}$ is assumed to be 3 kg/s at the maximum heat produced, the temperature

difference between the inlet and the outlet of the coolant channel can be obtained:

$$\Delta T = T_{st,c,out} - T_{st,c,in} = 12\,K \tag{33}$$

The cooling capacity of the radiator at a maximum fan speed should remove the heat produced in the stack under circumstances where the bypass valve in the thermal system is closed and the coolant flows to the radiator. Figure 12 shows the relationship between the heat transfer coefficient and the air flow at a radiator [19].
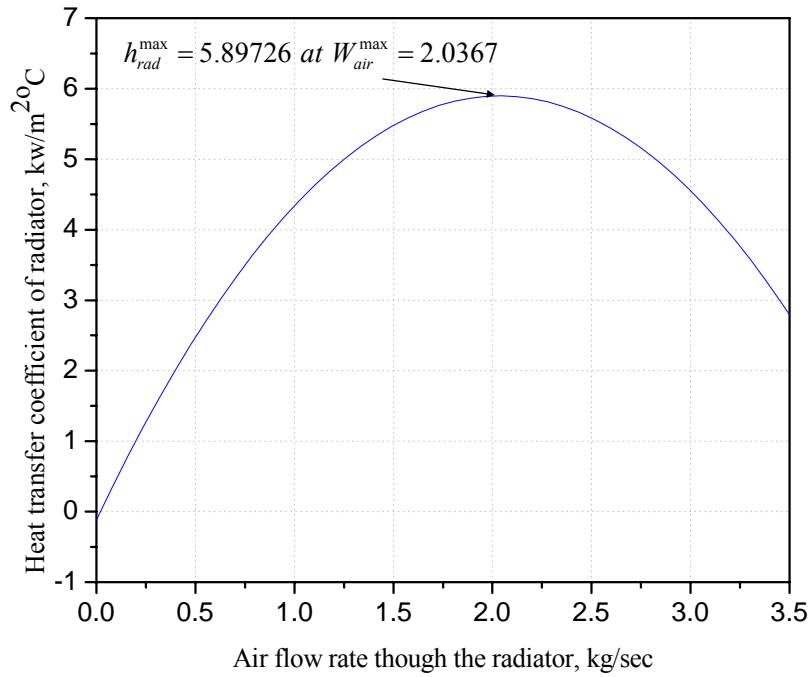

Figure 12 Heat transfer characteristic for the radiator

Using the heat transfer coefficient obtained at the maximum fan speed, the frontal area of the radiator is 1 m^2 (Eq. 15). The parameters used for the following analyses are summarized in Table 3.

Parameter	Value	Unit	Parameter	Value	Unit
i_{max}	1	A·cm^{-2}	T_{amb}	298.15	K
$W_{c,max}$	3	kg·s^{-1}	$h_{rad,max}$	5.89726	kW·m^{-2}·$^{\circ}$C^{-1}
Cp_c	4178	J·kg^{-1}·K^{-1}	Fr	1	m^2
ΔT	12	K	m_{res}	5	kg

Table 3 Parameters for the thermal circuit

4.2. DESIGN OF COOLANT CONTROL

Figure 13 depicts the design of a block diagram for the air supply system and thermal circuit with two different controls. The first uses two linear PI controllers for the coolant flow rate and the temperature in the reservoir with two compensators. The second is designed with a state feedback controller for both control loops with the same compensators.
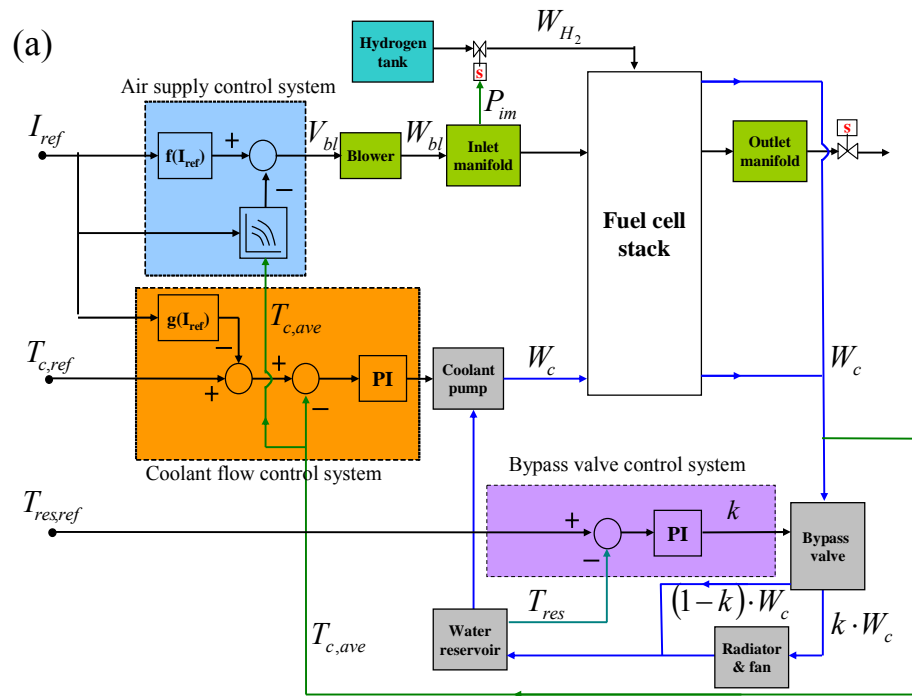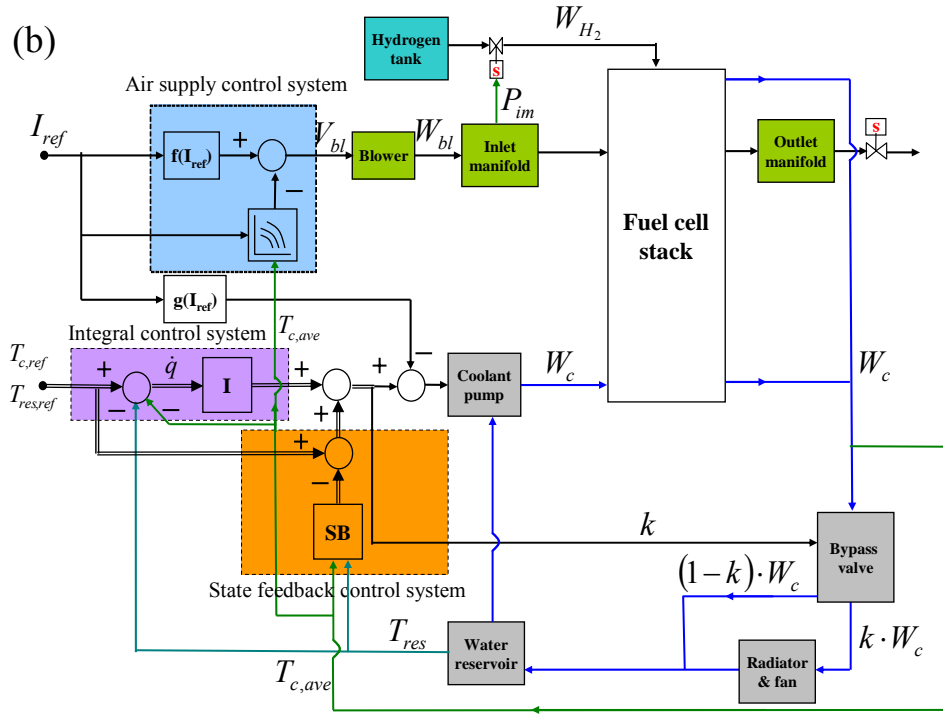
Figure 13 Block diagram for air and coolant control with (a) classic PI controllers and (b) state feedback controller with integral controller

4.2.1. DESCRIPTION OF STACK

The thermal mass and heat capacity of the stack depends upon how the stack is constructed. If it is assumed that all of the cells for a stack are identical, a stack can be modeled by using a single cell or a two-cell stack characteristic as shown in Figure 14. The two cell stack is more realistic because the effects of an adjacent cell on the performance can be reflected.
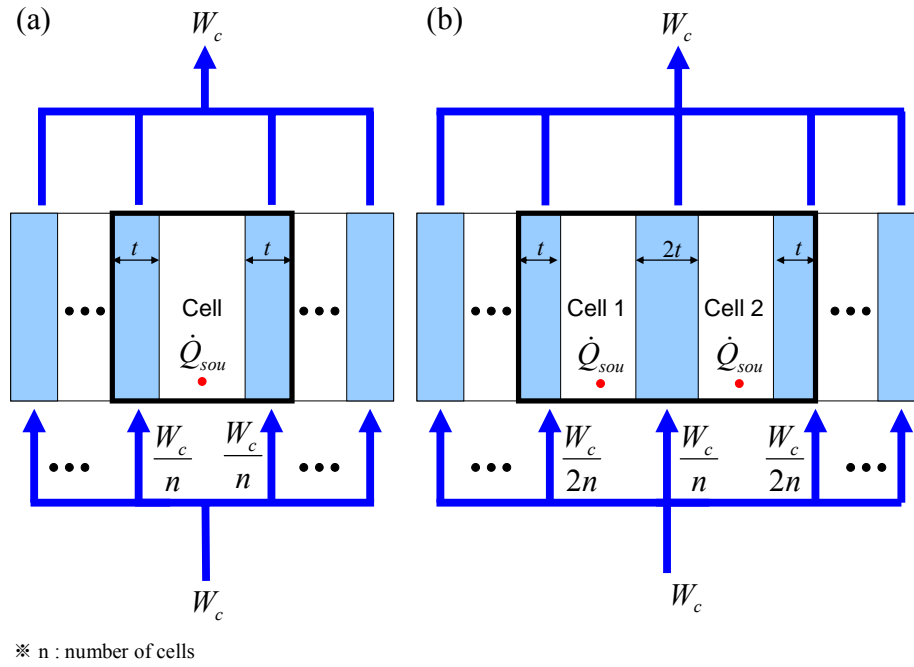
Figure 14 Schematic diagram of a stack for temperature controls based on (a) a single cell and (b) a two-cell stack

Under the assumption that the heat exchange by radiation is negligible and the stack temperature is equal to the average of the stack outlet coolant temperatures on the anode and cathode sides, the variation of the temperature in the stack is equal to the sum of the heat source terms in the stack, the heat exchanged with the coolants, and the ambient air:

$$mCp_{st}\frac{dT_{st}}{dt} = \dot{Q}_{sou} + W_c \cdot Cp_c \cdot (T_{c,in} - T_{st}) + hA_{st} \cdot (T_{amb} - T_{st}) \tag{34}$$

Where mCp_{st} is the heat capacity of the stack ($J \cdot K^{-1}$) that is the sum of the heat capacities of individual layers, W_c is the coolant flow rate ($kg \cdot s^{-1}$) as the control variable, and $\dot{Q}_{sou}$ is the internal energy source ($J \cdot s^{-1}$), a function of the load current.

37

4.2.2. THE PLANT MODEL FOR COOLANT CONTROL

Eq. 17 describes the temperature of the reservoir and can be modified to an equation that includes the bypass valve opening factor. The reservoir inlet coolant temperature is determined by the bypass valve opening factor, and the coolant temperature of bypassing and radiator outlet coolants:

$$
\begin{aligned}
& mCp_{res} \frac{dT_{res}}{dt} \\
& = W_c \cdot Cp_c \cdot ((1-k)\cdot T_{st} + k \cdot T_{rad,c,out} - T_{res,c,in}) + hA_{pl} \cdot ((1-k)\cdot T_{st} + k \cdot T_{rad,c,out} - T_{amb})
\end{aligned}
\tag{35}
$$

Because of the nonlinearity of the equations in the lumped thermal stack (Eq. 34) and the reservoir model (Eq.35), the Talyor's expansion is used for linearization at an operating point, where the reservoir temperature and coolant flow rate are set at 64°C and 0.93 kg/s, respectively, while the stack current and voltage are 140A and 198V, respectively. The state equations and variables are defined as follows:

$$
\begin{aligned}
\delta \dot{x} &= A \cdot \delta x + B_u \cdot u + B_w \cdot w \\
\delta y &= C \cdot \delta x
\end{aligned}
\tag{36}
$$

$x = \begin{bmatrix} T_{st} & T_{res} \end{bmatrix}$ (States)

$u = \begin{bmatrix} W_c & k \end{bmatrix}$ (Controlled input)

$w = I_{st}$ (Disturbance)

$y = \begin{bmatrix} T_{st} & T_{res} \end{bmatrix}$ (Output)

Where the matrices of the linearized system, A, B_u, B_w and C for a single cell and a two-cell stack are listed in Appendix B.

The plant shown in Figure 15 presents a second order linear system with a multi-input-multi-output (MIMO) structure. The input variables are the coolant flow rate and the valve opening of the bypass valve, while the states are both temperature in the stack and the reservoir, where both states are simultaneously manipulated by input variables. However, the element, Bu_{21}, is relatively small in comparison to the other, Bu_{22}, so that the former can be neglected and the temperature in the stack can be assumed to be only manipulated by the coolant flow. In the same way, the element, Bu_{12}, can be neglected and the temperature in the reservoir can be assumed to be only controlled by the bypass valve opening factor.
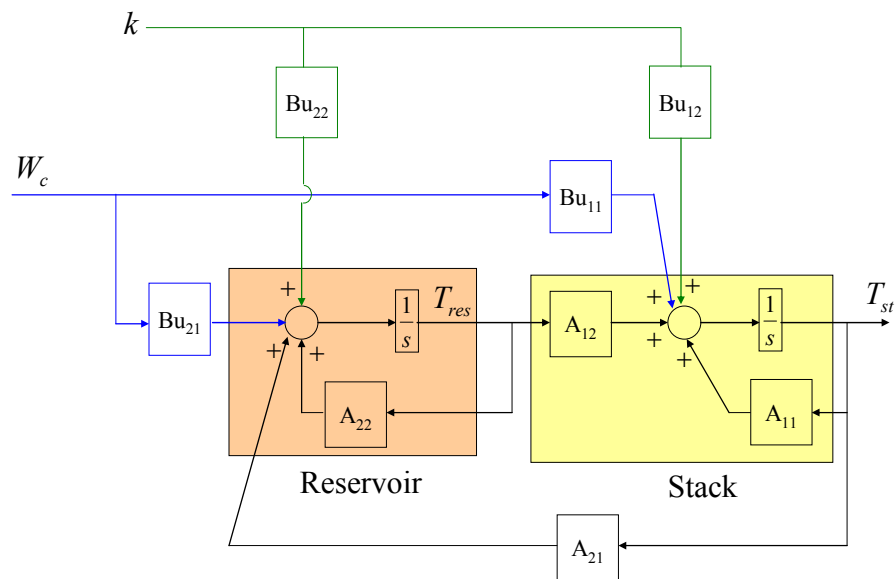

Figure 15 Block diagram of the plant for the coolant controls

4.2.3. DESIGN OF CLASSIC PI CONTROLS

The state equations derived above present a multi-input-multi-output structure, where two controlled input variables, coolant temperature and flow rate, are dependent upon each other. This dependence can be minimized if the time constants of two feedback loops are set in a different order. Thus, the temperature in the stack can be controlled by the coolant flow rate independent of the temperature of the coolant being controlled by the opening factor; k. Eq. 34 includes the relationship between the stack temperature and the coolant flow rate, the transfer function of which is given in Eq. 37. The system shows the first order of an ordinary differential equation, and thus a classic PI controller is employed. The two gains of the PI controller are selected by the bandwidth of the closed-loop that is 3 times higher than the time constant of the heat source term response, and a damping ratio of 0.707. The resulting gains are $K_{p,c} = 0.25$ and $K_{I,c} = 0.017$ (s^{-1}):

$$\frac{T_{st}(s)}{W_c(s)} = \frac{Cp_c \cdot \left(T_{res}^o - T_{st}^o\right)}{\left(mCp_{st} \cdot s + W_c^0 \cdot Cp_c + hA_{st}\right)} \tag{37}$$

$$G_{c1}(s) = K_{p,c} + \frac{K_{I,c}}{s} \tag{38}$$

Eq.17 includes a relationship between the temperature in the reservoir and the factor for the bypass valve opening, the transfer function of which is given in Eq. 39. Likewise, the gains for the PI controller are so selected that the bandwidth of the closed-loop is 5 times higher than the time constant of the coolant flow feedback outer loop. In addition, the damping ratio is set to 0.707. The resulting gains are $K_{p,b} = 0.1902$ and $K_{I,b} = 0.0546$ (s^{-1}):

$$\frac{T_{res}(s)}{k(s)} = \frac{\left(W_c^0 \cdot Cp_c + hA_{pl}\right) \cdot \left(T_{amb} - T_{st}^o\right)}{\left(mCp_{res} \cdot s + W_c^0 \cdot Cp_c\right)} \tag{39}$$

$$G_{c2}(s) = K_{p,b} + \frac{K_{I,b}}{s} \tag{40}$$

The transfer functions of the closed loop for the temperature in the stack and reservoir have one zero and two poles, respectively. The PI controllers for the inner and outer loop add a zero and a pole in the loop, so the dominant poles of the characteristic equations are located in the complex. Because the control system is a second order system, the poles of the closed-loop cannot be optimally positioned. The location of the zero and poles given by the plant and the design are shown in Figure 16 .
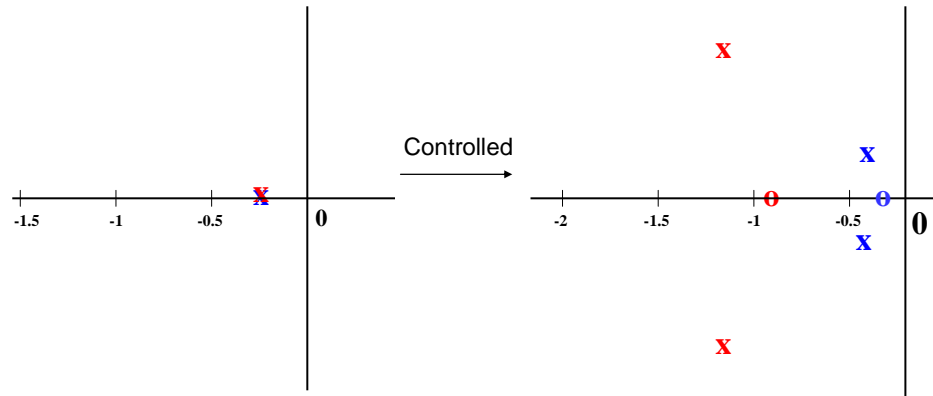
Figure 16 Location of changes of poles and zeros after PI controls

Because the plant is a linear system, the responses of the two states at a step where U_1 and U_2 are held constant are shown in Figure 17. This shows that the

41

temperature in the stack responds faster than that in the reservoir when the coolant flow rate is changed. Conversely, the valve opening factor influences the temperature in the reservoir more than that in the stack.
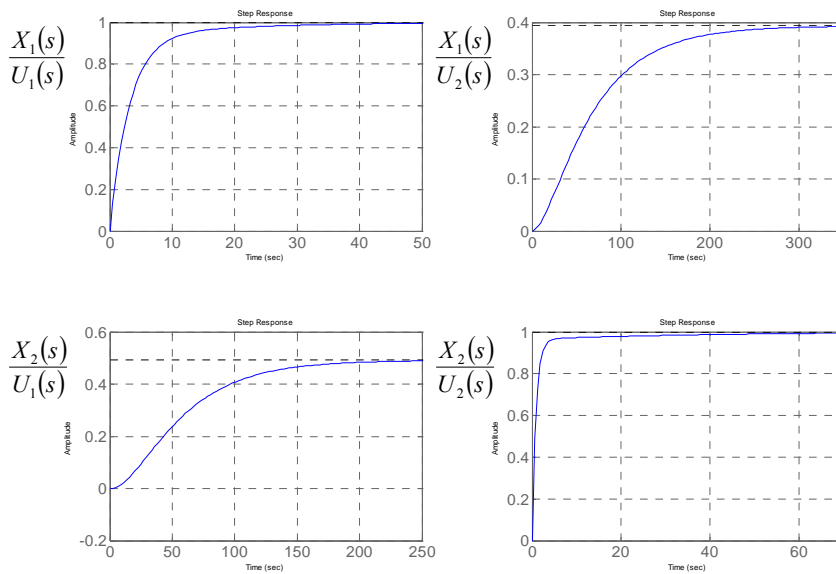

Figure 17 Step responses of the temperature in the stack and reservoir

4.2.4. DESIGN OF STATE FEEDBACK CONTROLS WITH INTEGRAL CONTROL

The classic PI controllers do not consider the parasitic power in the coolant pump as a control object, even though it rejects the heat and effectively suppresses temperature surges in the layers. One alternative is the use of a state feedback control, where the parasitic power dissipated in the coolant pump can be considered to be one of the control objectives. However, the parasitic power of the coolant pump is directly proportional to the coolant flow rate. Thus, the coolant flow rate is included as a parameter in the cost

function. The optimization of the gains is conducted by the LQR (linear quadratic regulator) method, which basically sums the square of the errors:

$$J = \int_0^\infty (\delta x^T Q_x \delta x + \delta u^T R \delta u) dt \qquad (41)$$

where Q_x represents the weighting matrix amplifying the errors of the control objects, while the other weighting matrix, R, is used to suppress the effect of the manipulating variables.

The state equation of the control plant presents a 2-by-2 matrix, in which variables are coupled to each other. A decoupling of the two loops was accomplished by assigning different time constants for the two closed loops. The valve opening factor does not directly affect the dynamics of the stack temperature, while the reservoir temperature is influenced by the valve opening factor rather than the coolant flow rate. Hence, the time constant of the transfer function between the stack temperature and coolant flow rate is set 5 times faster than that between the stack temperature and the valve opening factor. By contrast, integrators are required to suppress any steady state errors. Thus, the errors of both closed loops are defined as a new state variable that is considered in the cost function:

$$\dot{q} = \begin{bmatrix} T_{st}^* - T_{st} \\ T_{res}^* - T_{res} \end{bmatrix} \qquad (42)$$

$$J = \int_0^\infty (\delta x^T Q_x \delta x + q^T Q_I q + \delta u^T R \delta u) dt \qquad (43)$$

where Q_I is the weighting matrix for integrator.

The rules for the optimal control inputs are obtained as follows:

$$\delta u = -K\begin{bmatrix} \delta x & q \end{bmatrix}^T = -K_p \cdot \delta x - K_I \cdot q \qquad (44)$$

where the controller gain is $K = R^{-1} Bu'^T P$. The value P is the solution of the Algebraic Riccati Equation as shown below:

$$P \cdot A' + A' \cdot P + Q - P \cdot B'_u \cdot R^{-1} \cdot B'^T_u \cdot P = 0 \qquad (45)$$

where $A' = [A, 0; C, 0]$, $B_u' = [Bu; 0]$, $Q = diag(Q_x, Q_I)$ and R is given in Appendix C.

When the weighting matrix R is larger than the weighting matrix Q, the role of the coolant flow rate in the cost function is increased and subsequently the gains of the controller are chosen, which minimizes the parasitic power. Figure 18 shows the step response of the coolant flow rate, which is dependent upon the weighting factor. As the weighting factor increases, the control loop behaves like a highly damped system.
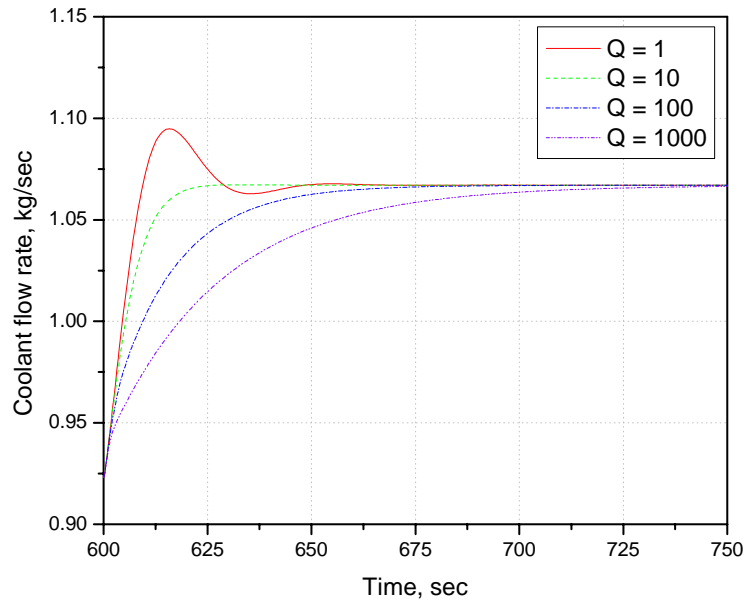

Figure 18 Step response of the coolant flow rate as a function of the weighting factor

After several iterations with different weighting factors, the optimal control matrix K_p and K_I for the single cell stack with $Q = 10$ is obtained:

$$K_p = \begin{bmatrix} -1.2015 & 0.01 \\ -0.0521 & -3.1479 \end{bmatrix}, \quad K_I = \begin{bmatrix} -0.1 & 0.0027 \\ -0.0027 & -0.1 \end{bmatrix} \quad (46)$$

The step responses of the temperature in the stack and reservoir after state feedback control is applied are shown in Figure 19. The response of bypass valve opening is faster than that of the coolant pump.
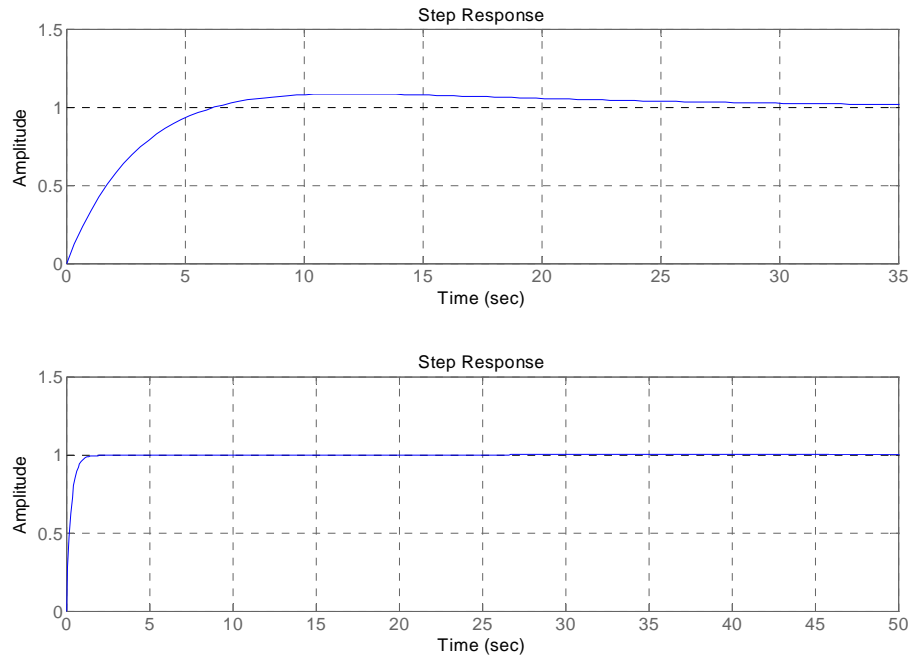

Figure 19 Step responses of the temperature in the stack and reservoir

4.2.5. DISTURBANCE COMPENSATION

The heat produced in the stack tends to follow the current drawn from the stack. The current-dependent heat is regarded as a disturbance in the control loop, which cannot

45

be fully rejected by the typical coolant control that measures the temperature at the outlet of the coolants. As a result, the heat rejected is less than the heat produced. A countermeasure is to estimate the temperature rise in a layer that is directly related to the magnitude of the current load and feed-forward it to the temperature control loop shown in Figure 13. The relationship between the current and the stack temperature is derived by using Eq. (8) and Eq. (19) yielding the following transfer function (Eq. 47), where v_{act} represents the activation over-potential:

$$\frac{T_{st}(s)}{I(s)} = \frac{\left(-\dfrac{T\Delta s}{4F} + v_{act}\right)}{\left(m_{st}Cp_{st} \cdot s + Cp_c W_c^0 + hA\right)},$$

$$\frac{T_{st}(s)}{I^2(s)} = \frac{R_{membr}}{\left(m_{st}Cp_{st} \cdot s + Cp_c W_c^0 + hA\right)}$$

(47)

However, all previously published air supply control designs assumed a constant working temperature of the cell. Here, the temperature distribution in the individual layers through the plane varies because of the various sources of heat associated with the chemical reactions and Joule's losses associated with charge transport. In order for rejection of the heat in the stack to occur, the temperature of the coolants control loop must be set lower than that in the stack, which changes the temperature in the gas flow channels. When the temperature in the gas flow channel is lower, the pressure drops according to the ideal gas law for the given volume and then the pressure difference at the inlet manifold becomes larger. However, the mass flow rate at the inlet of the stack increases according to the nozzle equation and consequently the oxygen excess ratio is increased. The surplus air is reduced by an additional element in the controls that depends upon the coolant temperatures in addition to the current that determines the amount of

oxygen consumed. Because of the nonlinear relationship between the blower voltage and different currents and temperatures at the optimum oxygen excess ratio, a set of data is obtained from multiple runs of the entire model under different currents and temperatures, which are used for a compensation of the effects.

4.3. SIMULATION AND ANALSES

Simulations were performed to analyze the dynamic behavior of the stack along with the air supply, thermal system, and the associated control strategies. Thus, the one cell and two cell stack models were developed. Dynamics of water content in the membranes, temperature variations, oxygen excess ratio, and responses at the load currents are analyzed in the following sections. The geometrical data for layers are as follows (Table 4) [6]. All models were coded by blocks given in MATLAB/Simulink.

|	Thickness m	Density $W\,m^{-1}K^{-1}$	Heat conductivity $J\,kg^{-1}K^{-1}$	Specific heat $kg\,m^{-3}$
Coolant Channel	0.002	1400	30	935
Plate	0.001	1400	52	935
Gas Channel	0.001	1400	52	935
GDL	0.0004	2000	65	840
Catalyst layer	0.000065	387	0.2	770
Membrane layer	0.0001275	1967	0.21	1100

Table 4 Geometrical data for layers

4.3.1. SIMULATION ON THE BASIS OF A SINGLE CELL STACK

4.3.1.1. WATER CONTENTS IN THE MEMBRANE

Figure 20 shows a comparison of the membrane water content between the empirical model and the proposed model at a step load current. The membrane water

content primarily depends upon the relative humidity, which is determined by the saturated vapor pressure and depends on the temperature and vapor pressures of both the cathode and anode sides. Since the empirical model assumed a constant temperature of 80° C in the membrane, no dynamics of water transfer is involved and subsequently the vapor pressure only follows the change of the load current. Conversely, the temperature strongly influences the water content in the membrane. In particular, the water content becomes higher when the temperature of the catalyst layer on the cathode side is controlled at 80   and the temperature of the gas channel is <80° C. Under these conditions, the saturated vapor pressure decreases and relative humidity becomes higher. In addition, the elevated temperature of the stack caused by a high load current leads to a high saturated vapor pressure and a low relative humidity on both sides of the cell. As a result, the membrane water content is decreased.
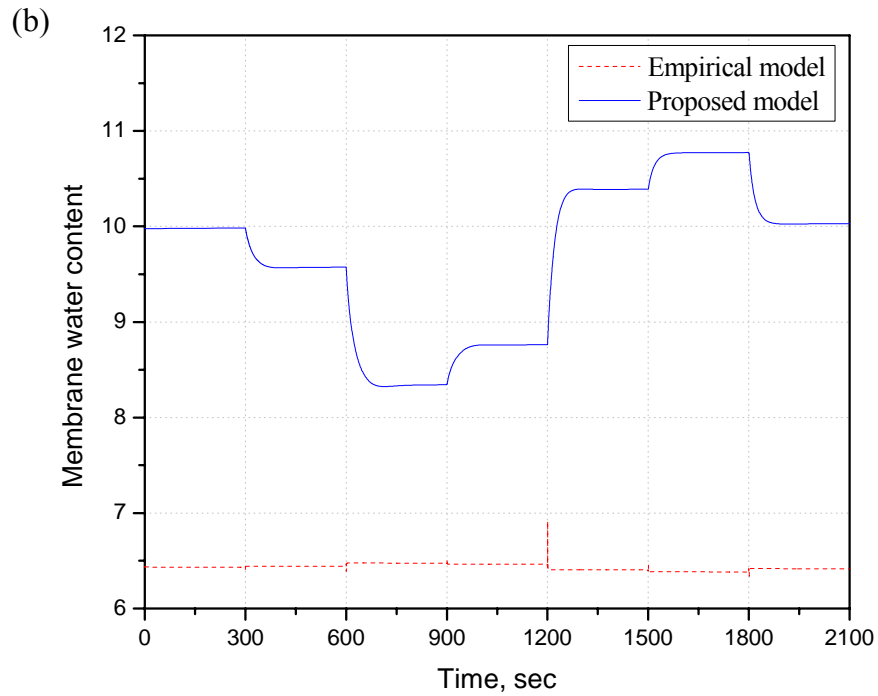
(a)

(b)
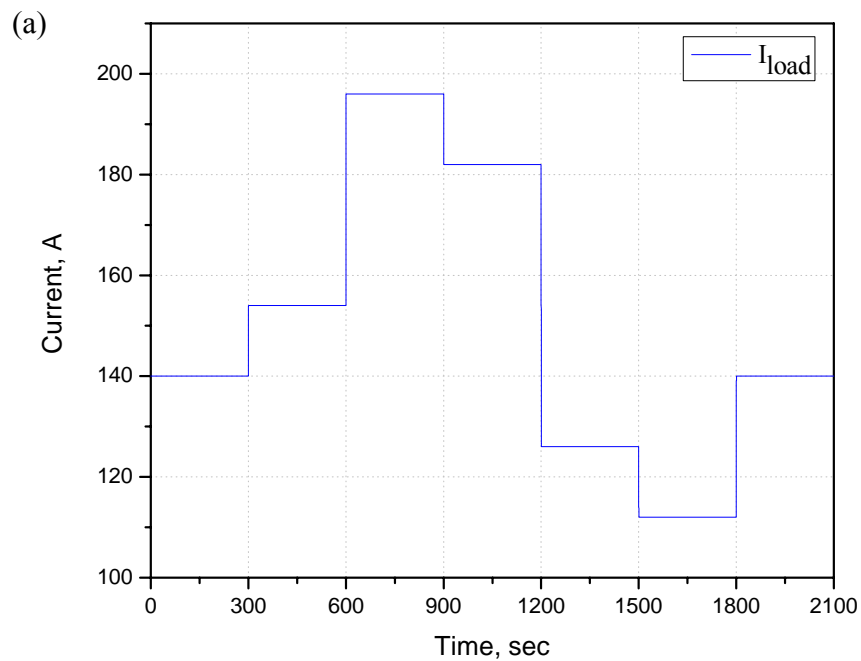
Figure 20 (a) Current and (b) water content in the membrane

4.3.1.2. TEMPERATURE IN THE CELL

When a multi-step current is applied to the stack, the temperature in the stack rapidly rises, particularly in the catalyst on the cathode side. The temperature rise is 3~7° C higher than the average temperature in the stack, where the coolant temperature is fully controlled for the reference temperature 76°C (see the dotted line in the Figure 21). It should be noted that the catalyst and membrane layers should not be overheated because they might be damaged.

The temperature difference in the layers can be reduced by a feed-forward (FF) of the disturbance to the coolant control loop that should reject this excessive heat quickly.

The transfer function of the disturbance is given in Eq. 46. The result of the control strategy proposed is illustrated in Figure 21 with a straight line, where the temperature of the catalyst layer is maintained at ~80°C. The coolant temperature reflects the variation of the catalyst temperature. However, the instantaneous rise of the temperature cannot be fully suppressed because of the high thermal mass and large heat capacity of the stack. In addition, a steady state error is caused by the temperature difference between the coolant channel measured and the catalyst layer. Nevertheless, the cooling of the cell is effective and the duration of the heat on individual layers can be minimized.
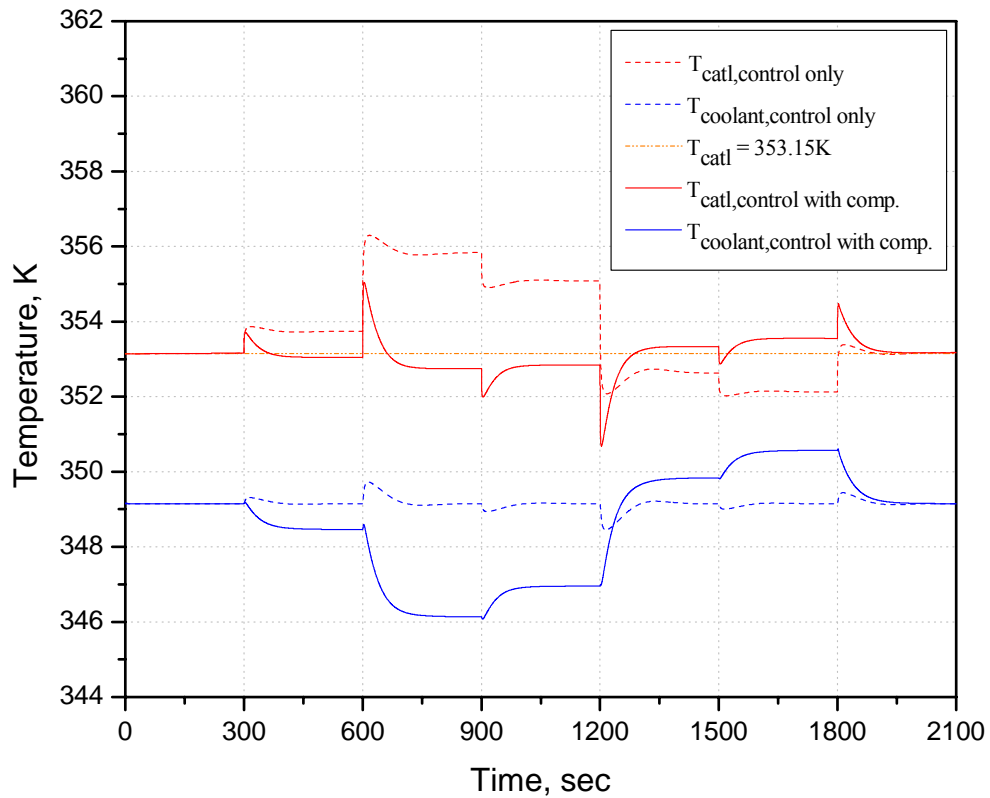

Figure 21 Temperature of the catalyst layer and coolant channel as a function of the coolant flow controls

The effects of the coolant controls on temperature distribution through the plane of a cell are shown in Figure 22. As the amplitude of the current density changes stepwise from $0.5A/cm^2$ to $0.55A/cm^2$, or from $0.65A/cm^2$ and $0.7A/cm^2$, the stack temperature becomes higher. When the feed-forward is applied, the overall stack temperature becomes lower and the catalyst temperature in the cathode is maintained at 353.5K, which is significantly lower than before compensation applied. Likewise, the maximum temperature change between the catalyst at the cathode side and the coolant channel is 6K lower. As a result, the cooling of the stack becomes more effective.
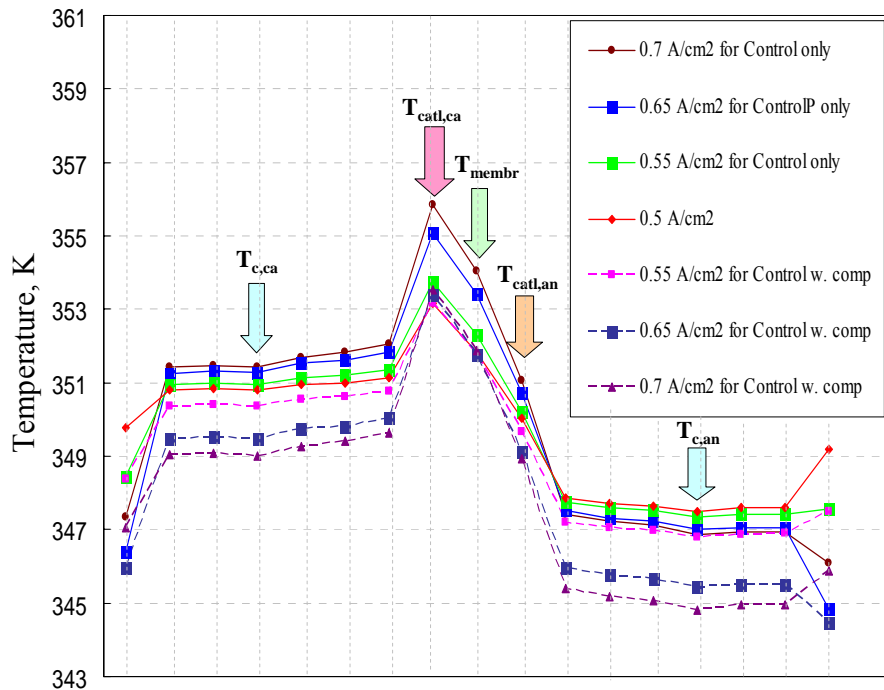

Figure 22 Temperature variations in a cell depending on currents with and without feed-forward of the disturbance

4.3.1.3. OXYGEN EXCESS RATIO

The oxygen excess ratio at a constant and dynamically varying temperature with a coolant flow control is illustrated in Figure 23. Because variation of the stack temperature causes changes in the pressure in the gas flow channel, the oxygen excess ratio is inversely influenced by the direction of the current changes.
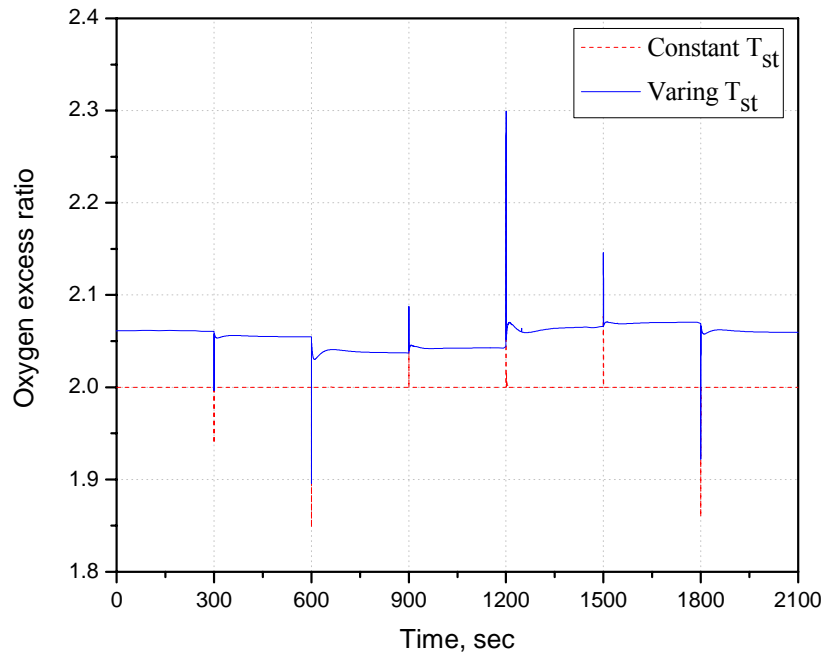

Figure 23 Comparison of the oxygen excess ratio at a constant and varying temperature

A comparison of the oxygen excess ratio before and after a compensation of the temperature influence on the air control loop is shown in Figure 24. The compensation allows the oxygen excess ratio to be maintained at a value of 2, even though the current applied to the stack varies stepwise. This implies that the parasitic power at the blower is lower.
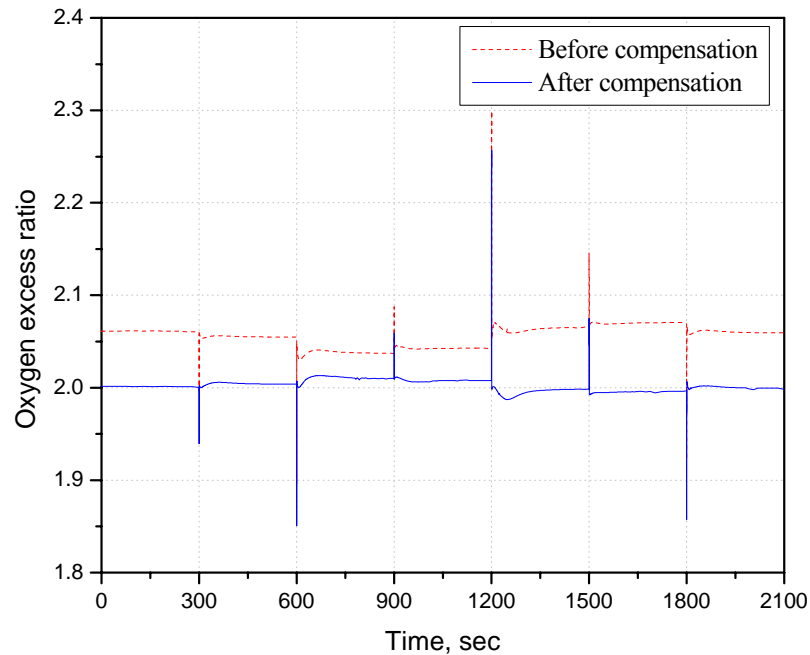
Figure 24 Comparison of the oxygen excess ratio before and after temperature compensation

4.3.1.4. COMPARISION OF THE PI AND STATE FEEDBACK CONTROLS

Comparison of both controls shows that the parasitic power of the state feedback controls at a multi-step current load is 5% less than that obtained using the PI controls. However, the dynamic response is much improved by the state feedback controls. In Figure 25, step responses of the two controls are simulated using the models described. The output states are the coolant flow rate and the stack inlet coolant temperature. The rise time of the coolant flow rate by the state feedback controller is 6 s, which is 4 times faster than that obtained using PI controls. Likewise, the rise time of the stack inlet coolant temperature is 3 times faster than that of the PI controller.
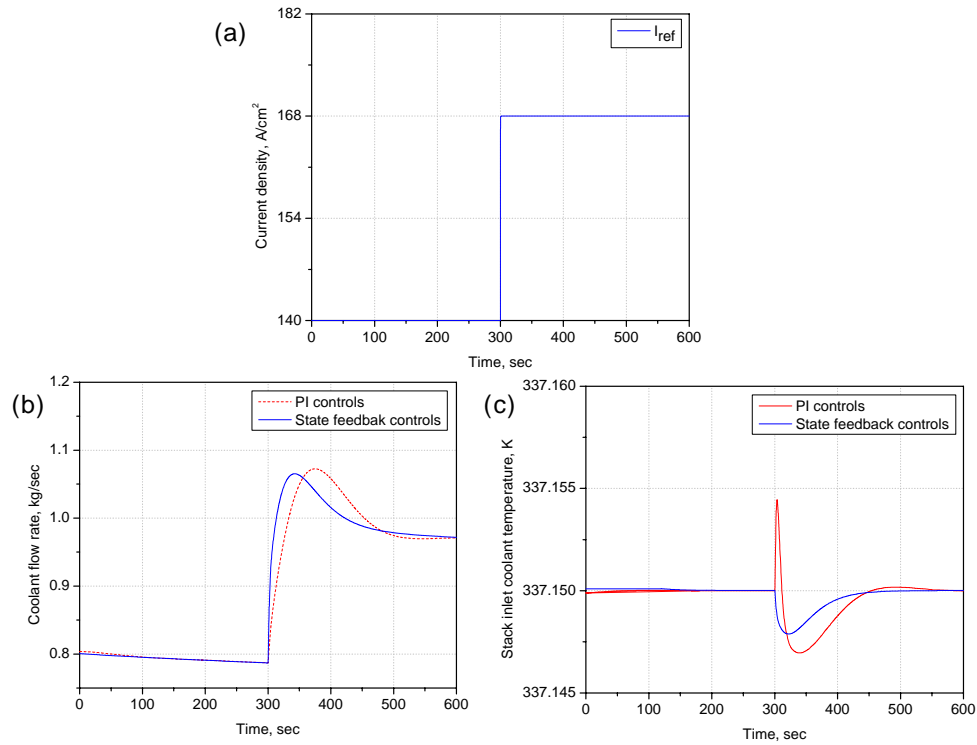
Figure 25 Comparison of (a) step current, (b) coolant flow rate and (c) stack inlet coolant temperature with a given current step between PI controls and state feedback controls

Parasitic power is calculated as the sum of the electrical power needed for driving the blower and the coolant pump. The control strategies with the state feedback control proposed requires 270Wh at the multiple step current, while that obtained without considering a valve and a PI control loop for the coolant requires 295Wh, as shown in Figure 26.
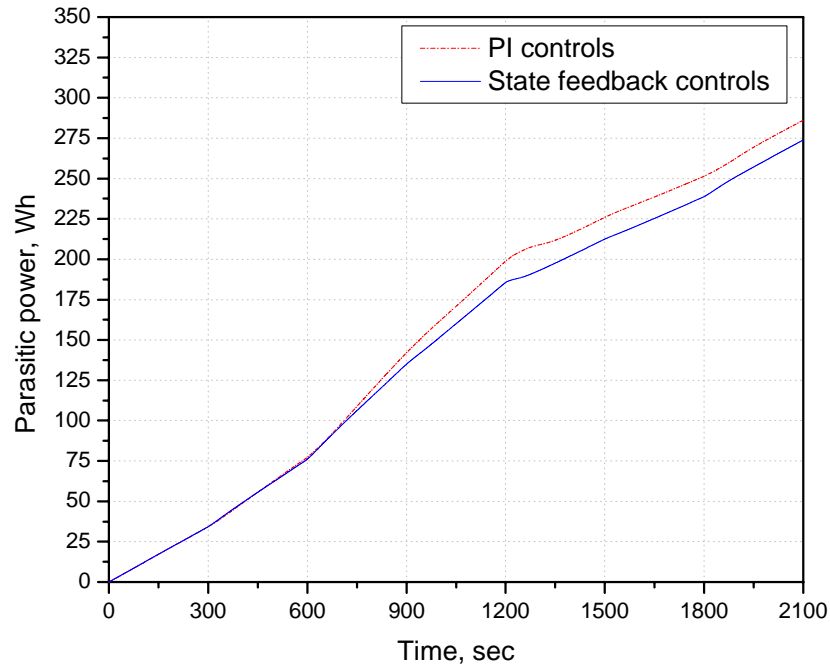
Figure 26 Comparison of accumulated total parasitic power between the PI and state feedback controls at a given load current step

4.3.2. SIMULATION AND ANALYSES ON THE BASIS OF A TWO-CELL STACK

Figure 27 shows the temperature distributions through the plane of the two cells when a state feedback controller with or without feed-forward control of the disturbance is applied. When the current density increases from $0.5A/cm^2$ to $0.7A/cm^2$, the temperature in the catalyst layer of cell 1 is higher than that in cell 2. After the feed-forward control of the disturbance is applied, the overall stack temperature becomes lower and the temperature in the catalyst of cell 1 is maintained around 353.5K, where the maximum temperature difference in the catalysts of cell 1 and cell 2 is 5K.
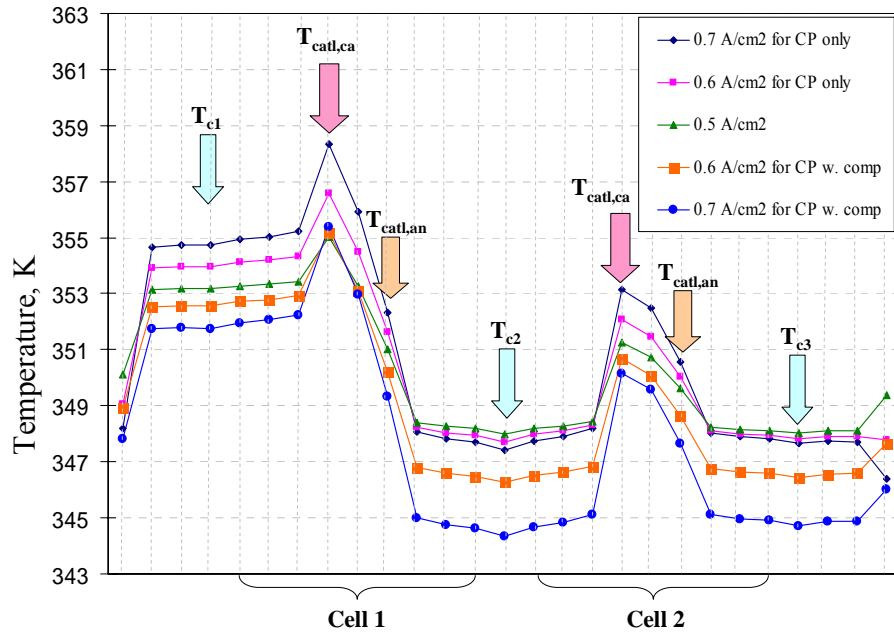
Figure 27 Temperature distributions in two cells with and without feed-forward control of the disturbance

The effects of controls on the water content in the membrane are shown in Figure 28a. In general, the membrane water content is influenced by the relative humidity on the cathode and anode sides. Even though the reactants on the anode and cathode sides are supplied with full humidification, the relative humidity (RH) in the gas channels on the anode side of the cells drops because of the influence of the temperature on the gas flow channels. Since the temperature in cell 1 drops more than that in cell 2, because the coolant flow in the middle coolant channel is twice higher than those in the side coolant channels, the RH in cell 1 becomes higher than that in cell 2. Consequently, the water content in the membrane of cell 1 is slightly higher than that in cell 2.

In fact, the proton conductivity in the membrane depends on the water content and temperature ([12] and [13]). High proton conductivity reduces the ohmic over-potential and subsequently the cell voltage is increased. In addition, the water content in the membrane and the temperature of cell 1 is higher than that of cell 2, as shown in Figure 27 and Figure 28a. Consequently, the voltage of cell 1 becomes higher than that of cell 2 as shown in Figure 28b. The dynamic behavior of the stack voltage follows the dynamics of the water content in the membrane.
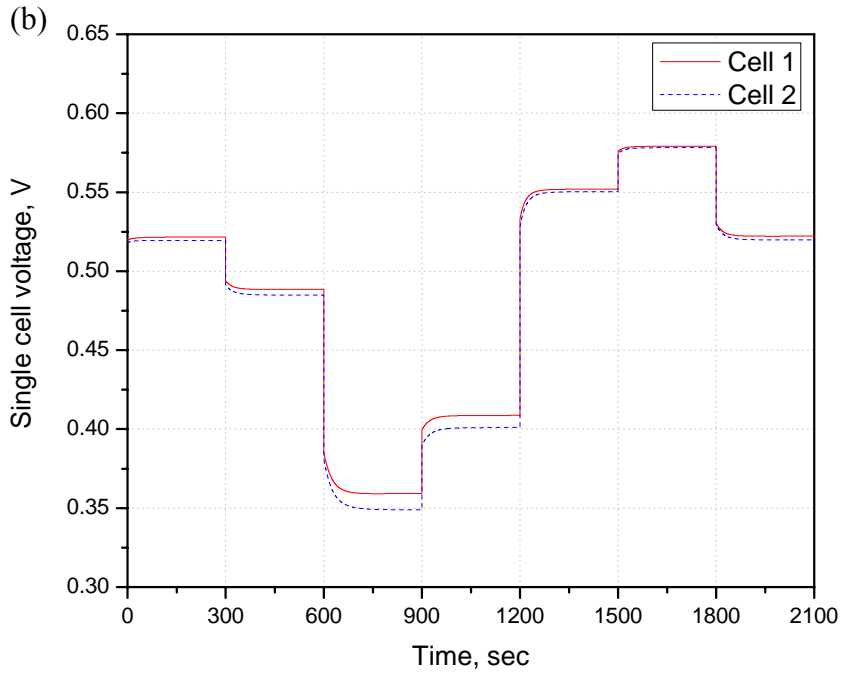
(a)

57

(b)
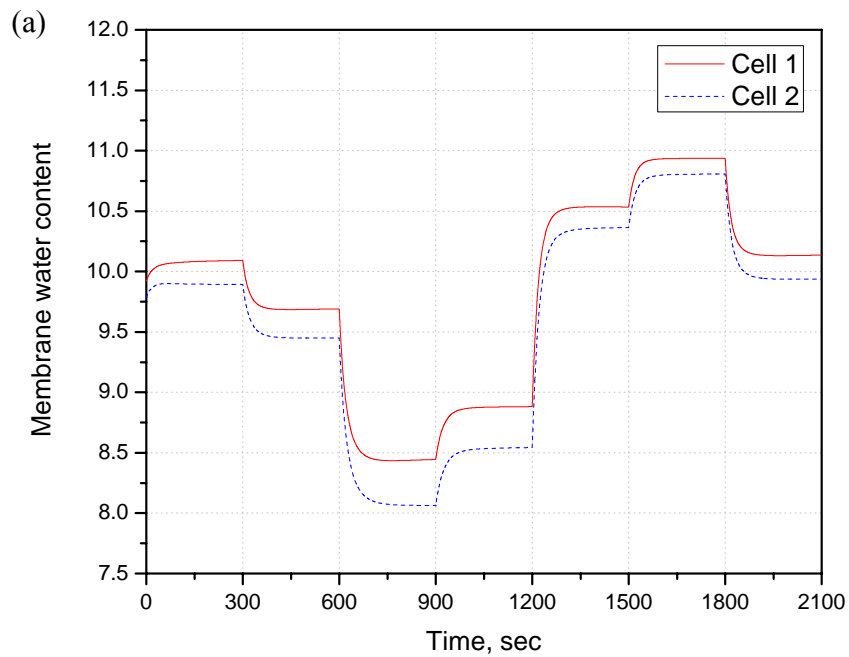
Figure 28 Comparison of (a) Membrane water content and (b) Single cell voltages between cell 1 and cell 2

4.3.3. RESPONSE OF STATE FEEDBACK CONTROL WITH FUDS

The response of the state feedback control was compared to a conventional control by using a current profile obtained from a vehicle tested at the Federal Urban Driving System (FUDS). Figure 29 shows the simulation results for the two different control strategies at a given current. The peak temperature in the catalyst layer is 6K higher than the working stack temperature by using the control without the FF, even though the coolants are controlled around the set reference temperature shown in Figure 29b. Figure 29c shows the temperature of the catalyst and coolants with the FF of the disturbance. The peak of the temperature is similar to the others for the first 200 s, but is suppressed in the following intervals as compared to Figure 29b. The excursion duration

58

of the catalyst temperature becomes less and finally the heat energy imposed on the thin layers is reduced, which significantly reduces the heat stress on the layers. Correspondingly, the oxygen excess ratio is maintained at the optimum value by the compensation shown in Figure 29d.
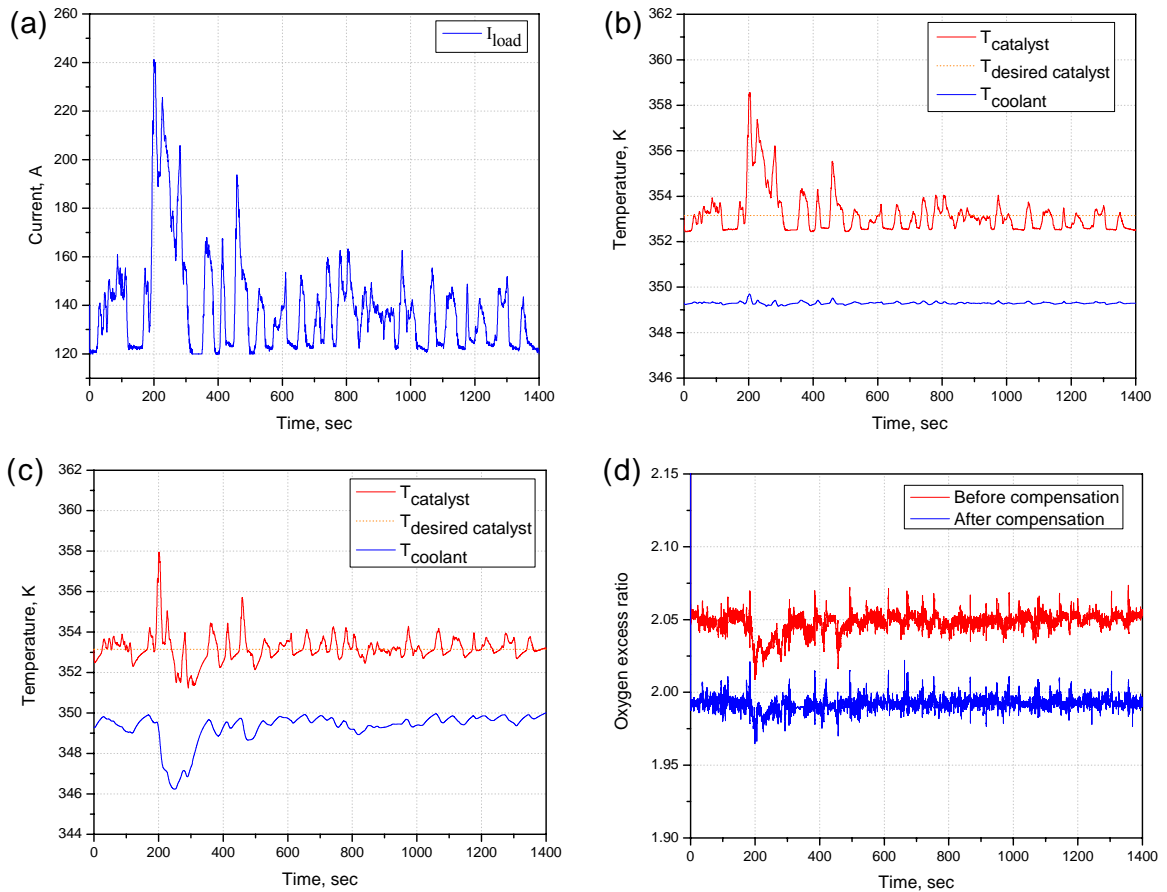

Figure 29 (a) FUDS and a current profile with a base load of 120 A, (b) temperature of the catalysts and coolants without the FF, (b) temperature of the catalysts and coolants with the FF, and (d) Oxygen excess ratio after temperature compensation

5.   CONCLUSION AND FUTURE WORK

The research presented addresses the design of temperature control strategies for PEM fuel cells and presents an analysis of the effects on dynamics and performance. The fuel cell control is assessed by using a dynamic stack model that includes gas diffusion in GDL, the dynamic water balance in the membrane, temperature variation, and components of the air supply and thermal system. The major outcomes are summarized as follows:

- The proposed model improves dynamic stack behavior by adding analysis of the dynamic water balance in the membrane, the partial pressure drop in the GDL, and temperature distributions. The results show that distribution of the temperature through the plane is asymmetric and the temperature rise amounts to 3-7°C that can potentially damage the layers at a high current load. Therefore, proper control of the air and temperature might be required to ensure the durability and increase the efficiency of the fuel cell;

- Most other control strategies have focused on optimization of the air supply system, where the working temperature in the fuel cell stack is presumed to be constant. However, we found that the oxygen excess ratio varies inversely as the temperature changes. Thus, the ideal oxygen excess ratio necessary for the prevention of oxygen starvation cannot be maintained at the optimum value of

2;

- The disturbance and compensator are used to minimize the temperature effect on the air flow rate. For design of the temperature controller, the thermal circuit was approximated with a second order system. Classic PI and state feedback controls were used to compare the effectiveness of the cooling. The results showed that the temperature rise in the catalyst could be maintained within an allowable value and duration. In addition, the oxygen excess ratio was maintained at an optimal value by minimizing the influence of temperature variations in the gas flow channel. Consequently, the power consumption of the blower was reduced >15% by the compensation and 5% by the controlling coolant pump and bypass valve at a multi-step load profile. Final reduction of the total parasitic power for the air and coolant control loop was ~7%.

Future work will include analysis of the following issues: 1) design of an observer for the temperature in the layers using advanced controls and real-time diagnosis as well as the water content in the membrane, and 2) optimization of the air and temperature controls under the influence of a humidifier.

REFERENCES

[1] Larminie, J. and Dicks, A., *"Fuel Cell Systems Explained,"* 2nd ed., Wiley, 2003.

[2] Pukrushpan, J. T., Peng, H. and Stefanopoulou, A.G., *Simulation and Analysis of Transient Fuel Cell System Performance based on a Dynamic Reactant Flow Model*, Proc. of IMEXE'01, 2002 ASME International Mechanical Engineering Congress & Exposition, New Orleans, LA, 2002.

[3] Shan, Y. and Choe, S. Y., *A High Dynamic PEM Fuel Cell Model with the Temperature Effects,* J. Power Sources, vol. 145, no. 1, pp. 30-39, 2005.

[4] Krause P. C. and Wasynczuk, O., *"Electromechanical Motion Devices,"* first ed., McGraw-Hill Book Company, New York, 1989.

[5] Ceraolo, M., Miulli, C. and Pozio, A., *Modeling static and dynamic behavior of proton exchange membrane fuel cells on the basis of electro-chemical description,* J. Power Sources, vol. 113, pp.131-144, 2003.

[6] Gurski, S., *Cold Start Effects on Performance and Efficiency for Vehicle Fuel Cell System*, Master of Science Thesis, Virginia Polytechnic Institute and State University, 2002.

[7] WÖhr, M., Bolvin, K., Schnurnberger, W., Fischer, M., Neubrand, W., and Eigenberger, G., *Dynamic modeling and simulation of a polymer membrane fuel cell including mass transport limitation*, Int. J. Hydrogen Energy, vol. 23, no. 3, pp. 213-218, 1998.

[8] Amphlett, J. C., Baumert, R. M., Mann, R. F., Peppley, B. A. and Roberge, P. R., *Performance modeling of the Ballard Mark IV solid polymer electrolyte fuel cell*, J. Electrochem. Soc., vol.142, no. 1, pp. 9-15, 1995.

[9] Rodtz, P. Paganelli G, Guzzella L., *Optimizing air supply control of a PEM fuel cell system*, Proceeding of the American Control Conference, Denver, CO, June, pp. 2043-9, 2003.

[10] Pukrushpan J. T., Stefanopoulou A. G. and Peng H., *Modeling and control for PEM fuel cell stack system*, Proceedings of the American Control Conference, Anchorage, Alaska, May 8-10, 2002

[11] Kroger, D.G, *Radiator Characterization and Optimization,* SAE paper 840380, 1984.

[12] Guzzella, L., *Control Oriented Modeling of Fuel-Cell Based Vehicles,* Presentation in NSF Workshop on the Integration of Modeling and Control for Automotive System, 1999.

[13] Pischinger, S., Schönfelder, C., Bornscheuer, W., Kindl, H. and Wiatalla, A., *Integrated Air Supply and Humidification Concepts for Fuel Cell Systems,* SAE paper 01 0233, 2001.

[14] Muller, E. A. and Stefanopoulou, A. G., *Analysis, Modeling and Validation for the Thermal Dynamics of a Polymer Electrolyte Membrane Fuel Cell Systems,* ASME Journal of Fuel Cell Science and Technology, accepted, also in Proceedings of the ASME 3rd International Conference on Fuel Cell Science, Engineering and Technology, FUELCELL2005-74050, 2005.

[15] Rodatz, P., Paganelli, G. and Guzella, L., *Optimization air supply, control of a PEM Fuel Cell system,* IEEE Proc. American Control conference, 2003.

[16] Pukrushpan, J. T., Stefanopoulou, A. G. and Peng, H. *Modeling and Control for PEM Fuel Cell Stack System,* Proceedings of the American Control Conference, Anchorage, AK pp. 3117-3122, 2002.

[17] Vahidi, A., Stefanopoulou, A.G. and Peng, H., *Model Predictive Control for Starvation Prevention in a Hybrid Fuel Cell system*, IEEE Proc. American Control conference, 2004.

[18]Anderson, B. D. O. and Moore, J. B., "*Optimal control: Linear Quadratic Methods*," Prentice-Hall, NJ, USA, 1989.

[19] Springer, T. E., Zawodzinski, T.A. and Gottesfeld, S., *Polymer Electrolyte Fuel Cell Model*, J. Electrochem. Soc., vol. 138, no. 8, pp. 2334-2342, 1991.

APPENDIX A

The matrices for the air supply system are obtained by linearization at the operating point.

$$
A = \begin{bmatrix}
-12.62 & 0 & -10.95 & 0 & 83.74 & 0 & 0 & 24.05 \\
0 & -161.9 & 0 & 0 & 51.64 & 0 & -18.12 & 0 \\
-37.57 & 0 & -46.31 & 0 & 275.7 & 0 & 0 & 158.3 \\
0 & 0 & 0 & -17.35 & 203.2 & 0 & 0 & 0 \\
2.598 & 0 & 2.968 & 0.3973 & -38.7 & 0.106 & 0 & 0 \\
33.28 & 0 & 38.03 & 5.0622 & -479.4 & 0 & 0 & 0 \\
0 & -449.5 & 0 & 0 & 142.1 & 0 & -80.83 & 0 \\
4.045 & 0 & 4.621 & 0 & 0 & 0 & 0 & -51.22
\end{bmatrix}
$$
,

$$
B_u^T = \begin{bmatrix} 0 & 0 & 0 & 3.946724 & 0 & 0 & 0 & 0 \end{bmatrix},
$$

$$
B_w^T = \begin{bmatrix} -0.03159 & -0.00398 & 0 & 0 & 0 & 0 & -0.05244 & 0 \end{bmatrix},
$$

$$
C_z = \begin{bmatrix}
4.94 & 2.091 & -1.089 & 0.1966 & 0 & 0 & 0 & 0 \\
-1.280 & 0 & -1.462 & 0 & 13.96 & 0 & 0 & 0
\end{bmatrix},
$$

$$
D_{zu} = \begin{bmatrix} -0.169 \\ 0 \end{bmatrix},
$$

$$
D_{zw} = \begin{bmatrix} 0.1802 \\ -0.01055 \end{bmatrix}.
$$

APPENDIX B

The matrices for the thermal management are obtained by linearization at the operating point.

$$A = \begin{bmatrix} -0.0245 & 0.0245 \\ 0.0373 & -0.0477 \end{bmatrix},$$

$$B_u = \begin{bmatrix} -0.3179 & 0 \\ 0.0089 & -2.4756 \end{bmatrix},$$

$$B_w = \begin{bmatrix} 6.34 \times 10^{-6} \\ 0 \end{bmatrix},$$

$$C = \begin{bmatrix} 1 & 0 \\ 0 & 1 \end{bmatrix}$$

APPENDIX C

The matrices for the state feedback and integral controller are obtained by linearization at the operating point.

$$A' = \begin{bmatrix} -0.0245 & 0.0245 & 0 & 0 \\ 0.0373 & -0.0477 & 0 & 0 \\ -1 & 0 & 0 & 0 \\ 0 & -1 & 0 & 0 \end{bmatrix},$$

$$B_u' = \begin{bmatrix} -0.3179 & 0 \\ 0.0089 & -2.4756 \\ 0 & 0 \\ 0 & 0 \end{bmatrix},$$

$$Q = \begin{bmatrix} 10 & 0 & 0 & 0 \\ 0 & 10 & 0 & 0 \\ 0 & 0 & 0.01 & 0 \\ 0 & 0 & 0 & 0.01 \end{bmatrix},$$

$$R = \begin{bmatrix} 1 & 0 \\ 0 & 1 \end{bmatrix}$$